

# **Micro and nano structure formation produced by fs laser ablation in reactive gas or liquid**

**Draft**

Master Thesis :

Marios Barberoglou

Τμήμα Θετικών Επιστημών  
Φυσικής  
Πανεπιστημίου Κρήτης

February 2009

Dedicated to my  
family and  
friends.

# Content

## **Chapter 1 – Overview**

1.1	Overview.....	1
1.2	Chapter content .....	4

## **Chapter 2 - Femtosecond laser microstructuring of crystalline Silicon**

2.1	Introduction.....	5
2.2	Formation mechanism. ....	6
2.3	Laser Induced Chemical Etching. ....	7
2.4	Experimental Setup .....	8
	2.4.1 The Ti:Sapphire laser system. ....	8
	2.4.2 Development of the Si spikes with the number of pulses.....	10
2.5	Fabrication of spikes under SF <sub>6</sub> (500 Torr).....	12
2.6	Conclusion.....	14

## **Chapter 3 - Theory of wettability**

3.1	Introduction .....	15
3.2	Contact Angle .....	16
3.3	Wettability and Surface roughness: Wenzel and Cassie-Baxter states. ....	17
3.4	Droplet motion on superhydrophobic surfaces .....	19
3.5	Restitution Coefficient.....	19

## **Chapter 4 – Tailoring the wetting response of silicon surfaces**

5.1	Induction. ....	21
5.2	Static CA measurement. ....	21
5.3	Morphology and static contact angle measurements. ....	22
5.4	Dimethyldichlorosilan (DMDCS) coating, and static CA measurements.....	25
5.5	Sliding Angle Experiments.....	27
5.6	Conclusion.....	32

## **Chapter 5 - Mimicing Nature : Learning from the Lotus Leaf**

<b>5.1</b>	Introduction.....	34
<b>5.2</b>	Preparation and study of the Structures .....	35
<b>5.3</b>	Bouncing experiments and analysis.....	38
<b>5.4</b>	Conclusion.....	42

## **Chapter 6 – Self Cleaning**

<b>6.1</b>	Introduction.....	43
<b>6.2</b>	Experimental.....	44
<b>6.3</b>	Self Cleaning on a titled surface.....	45
<b>6.4</b>	Water drop bounce with on dust covered surfaces	
	<b>6.4.1</b> Sample preparation.....	44
	<b>6.4.2</b> Bouncing experiments on dust covered surfaces.....	46
<b>6.5</b>	Conclusion.....	50

## **Chapter 7 – Reversible photoinduced wettability transition of hierarchical ZnO structures**

<b>7.1</b>	Introduction.....	51
<b>7.2</b>	ZnO nanostructured thin films.....	52
<b>7.3</b>	Experimental Details of ZnO nanostructured thin films.....	52
<b>7.4</b>	Reversible wettability of ZnO nanostructured thin films.....	53
<b>7.5</b>	Photoinduced wettability conversion mechanism.....	56
<b>7.6</b>	Hierarchical ZnO structures.....	58
<b>7.7</b>	Experimental Details of hierarchical ZnO structures.....	58
<b>7.8</b>	Reversible wettability of hierarchical ZnO structures.....	60
<b>7.9</b>	Contribution of roughness in the photoinduced transitions.....	64
<b>7.10</b>	Conclusion.....	67

## **Chapter 8 – Writing on bul Al via its ablation in air and liquids**

<b>8.1</b>	Introduction.....	69
<b>8.2</b>	Experimental procedure .....	70
<b>8.2</b>	Coloration of Aluminum.....	71
<b>8.3</b>	Formation of NS .....	74
<b>8.4</b>	Conclusions.....	76

# **Acknowledgements**

It is a pleasure to thank the many people who made this thesis possible.

It is difficult to overstate my gratitude to my Ph.D. supervisor, Dr. Emmanouil Stratakis. With his enthusiasm, his inspiration, and his great efforts to explain things clearly and simply, he helped to make research fun for me. Throughout my thesis-writing period, he provided encouragement, sound advice, good teaching, good company, and lots of good ideas. I would also like to thank Prof. Costas Fotakis who closely supervised this thesis

Special thanks go to Evi Papadopoulou and Dr. Emmanouil Spanakis for their contribution in a large part of this work and I am grateful to them for an excellent collaboration and many stimulating discussions

I am indebted to Aleka Manousaki and Sandra Siakouli for their continuous help with the SEM measurements as well as Alexandros Pagozidis for his experimental assistance.

Lastly, I would like to thank all my friends for their continuous support.

# Chapter 1

## 1.1 Overview

Femtosecond laser pulses open new research possibilities, allowing not only the observation of ultrafast phenomena, like chemical reactions, but also offering high energies for studying non-linear phenomena. Femtosecond laser pulses interact with mater allowing minimal thermal effects, producing micro/nano structures with desired properties.

This thesis consists of two parts. In the first and main part of this work, we will investigate the microstructuring on Silicon via laser ablation followed by a study of the wetting properties on these structured surfaces is made. In the second part a brief discussion is made on aluminum nanostructures and nanoparticles produced by fs ablation of Al in liquid media..

Silicon is widely used in microelectronic devices mainly due to its well defined characteristics and low cost. However,commercial silicon has its limitations. .For example it is transparent at wavelengths close to the NIR, which are mainly used in telecommunications (1,33 $\mu\text{m}$  and 1,55 $\mu\text{m}$ ), making the detection of these frequencies impossible. By laser structuring of the silicon we are able to overcome these difficulties and the produced micro roughness has new electrical and optoelectronic properties. In addition it shows enhanced wetting properties when water drops contact the structured surface.

Besides the electronic and optoelectronic properties, microstructuring of silicon gives rise to other important properties, such as wetting properties. We demonstrate the ability to change the surface from hydrophilic to hydrophobic, by measuring the corresponding contact angle of water drops sitting on surfaces with different roughness. A comparison with the Lotus leaf, one of the most famous water repellent plant surfaces, is also investigated.

The main part of the thesis is dedicated on the microstructuring of silicon via femtosecond laser irradiation. A systematic study has been made by irradiating flat crystalline silicon inside a vacuum chamber in the presence of 500 Torr SF<sub>6</sub> etching gas at different laser fluencies, varying from 0.33 - 2.25 J/cm<sup>2</sup> producing structures with different roughness. They exhibit a conical shape and their height,

density and geometry were calculated by corresponding scanning electron microscope (SEM) images.

By letting a nanopure water drop sit or roll on the silicon structured surfaces, we were able to measure the static contact and sliding angles and study the change in the wetting properties due to different surface roughness. The increasing surface roughness has a direct impact on the contact angle of the water droplet so that the surface changes from hydrophilic to hydrophobic. Following the ablation process the modified surfaces were covered by a hydrophobic coating rendering the surface superhydrophobic. Accordingly, a surface tilt of only  $4^\circ$  was enough to initiate the water drops motion for the roughest surface.

The dynamic behavior of water droplets free falling on flat or patterned surfaces as well as on those of the Lotus leaf was examined using a high-speed camera. The velocities before and after each shock were calculated either from the distance traveled between successive snapshots (at high impact speeds), or from the corresponding maximum heights attained (at low impact speeds). Self cleaning experiment have also been carried out, by covering the structured surface with carbon dust particles and letting a water drop roll or bounce on it.

The dynamic optical control/response of the wetting behavior of liquids was studied on hierarchically structured ZnO surfaces produced by depositing ZnO on the structured silicon surfaces by pulsed laser deposition (PLD). The final surface exhibits roughness at two-length scales comprising micrometer-sized Si spikes decorated by ZnO nano-protrusions. It is shown that a liquid droplet on these surfaces can be rapidly and reversibly switched between hydrophobicity and superhydrophilicity by alternation of UV illumination and dark storage or thermal heating. By studying the magnitude and the rate of the photoinduced transitions, the contribution of roughness at different scales is investigated in the framework of two theoretical wettability models.

In the second part on the thesis, the formation of self-organized nanostructures (NS) on bulk Al were studied when ablated by fs pulses either in air, or immersed in liquids. In the later case, the NS are regularly formed on the Al surface, independently of the laser polarization. Additionally, a dispersion of Al nanoparticles (NPs) into the liquid occurs and irregular nano-bumps are produced when the irradiation takes place in air. NP dispersions as well as NS

formed on Al surface show a characteristic absorption peak in the near UV which has been attributed to plasmon oscillation of electrons. The wings of this peak extending to the visible, lead to a distinct yellow coloration of the processed Al surface as well as the liquid dispersions. Ultrafast laser processing of bulk Al in liquids may be potentially a promising technique for efficient production of nanosized aluminum.

## 1.2 Chapter content

In **chapter 2** we will study the process of fs laser ablation of silicon under reactive gas atmosphere. The effect of different irradiation parameters on the attained morphology will be additionally analyzed.

In **chapter 3** we will briefly summarize the theory of wettability and define the terms hydrophobicity, hydrophilicity and contact angle. .

In **chapter 4** we investigate the wetting response of the laser structured silicon surfaces.

In **chapter 5** we will study the natural Lotus leaf and compare its structure and wetting properties with that exhibited by the structured surfaces.

In **chapter 6** we investigate the self cleaning ability of the artificial surfaces.

In **chapter 7** we will study the dynamic optical control of the wetting behavior of liquids on silicon structured surfaces coated with a pulsed laser deposited ZnO film.

Finally in **chapter 8** the formation of self-organized nanostructures (NS) on bulk Al were studied under its ablation in air and liquids with femtoseconds (fs) laser pulses.

# Chapter 2

## *Femtosecond laser microstructuring of crystalline Silicon*

### 2.1 Introduction

The interaction of laser irradiation with materials has been of scientific and technological interest since the development of the first lasers. <sup>[1]</sup>Absorption of laser irradiation by a solid can lead to a permanent modification of its surface, causing melting and resolidification, vaporization, or ablation of the material. Laser processing of solids, using both continuous and pulsed lasers, has been studied over the years for different classes of materials including metals, <sup>[2,3]</sup> semiconductors <sup>[4,5]</sup> and dielectrics. <sup>[6]</sup>

Structures on solids with pulsed lasers has been studied in different materials like metals, semiconductors and dielectrics, and the irradiation of silicon is able to produce periodical structures as in the case of LIPSS ( laser induced periodic surface structures).

The structuring of these surfaces with the help of nano/picosecond laser pulses has matured over the last 20 years, while the use of femtosecond pulses remains still a new method. The interaction of femtosecond pulses on solids differ from the nano/picosecond. In particular we are able to achieve low thermal effects and ultra fast phase changes, passing from the solid to the liquid and air phase.

In this chapter we examine the morphology, and structure (height, density) of the patterned Si samples fabricated using a femtosecond laser source, the effect of laser parameters (e.g. laser fluence and average number of pulses), as well as the roll of the reactive gas pressure ( $\text{SF}_6$ ), on the morphology of the structures obtained.

## 2.2 Formation mechanism.

The mechanism under which the formation of the conical structures occurs is complicated and hasn't been defined well. The most possible explanation is based on hydrodynamics. The first laser pulses melt a thin Si layer and as a consequence a different surface tension between the liquid and solid interface underneath is built. The development of complicated hydrodynamics phenomena lead to the formation of a wave like structure called capillary waves within the molten Si followed by resolidification that causes the formation of the imprinted wave on the silicon surface.

Upon further irradiation, the evaporated material condenses mostly on the top of the cones. The reason for this re-arrangement is the feedback between the surface morphology and its absorptivity (**Figure 2.1**). At homogeneous distribution of the laser beam intensity, the maxima of the temperature will be gained in those areas of the surface, which are oriented perpendicular to the laser beam axis. The latter angle corresponds to the incidence angle of laser radiation on the cone surface. This variation of the reflectivity provides the preservation of the conical structure at laser fluence close to the threshold of melting. In this sense the structures are self-organized ones. Moreover, laser radiation is reflected from the cones to the valleys between them (**Figure 2.1**), thus increasing the local laser fluence in the intercone area.

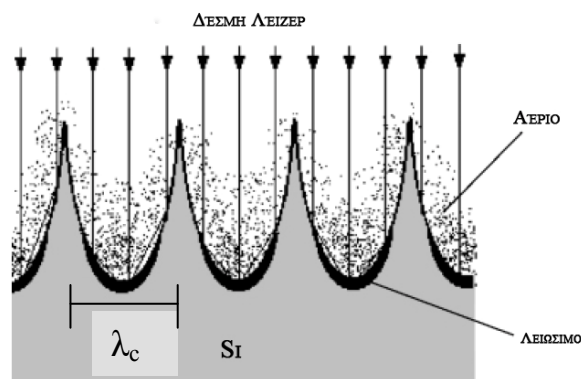


**Figure 2.1** : The schematic view of the development of the conical structure during laser evaporation. The black areas indicate the molten Si in the valleys during the laser pulse, while the cones remain solid.

The equation for the wavelength of the capillary waves that are formed at the beginning of the laser irradiation on the surface is :

$$\lambda_c = \left[ \frac{a \cdot d}{\rho} \right]^{1/4} \cdot (2 \cdot \pi \cdot \tau_c)^{1/2}$$

Were  $a$ : is the surface-tension coefficient of the air/liquid interface.

$d$ : thickness of the liquid.

$\rho$ : density of the liquid.

$\lambda_c$ : wavelength of the capillary waves.

$\tau_c$ : the period of the capillary wave.

### **2.3 Laser Induced Chemical Etching**

Chemical etching of a substrate can start or be enhanced with the help of a reactive gas. One of the most extensively used gases for etching of semiconductors, and in particular for Si, is SF<sub>6</sub> (Sulfur Hexafluoride), which is also used in the present thesis. The SF<sub>6</sub> is stable at 300 K and it is not chemisorbed on the surface at 90K or at pressures  $P > 1$  Torr at room temperature.

Laser induced etching of Si with SF<sub>6</sub> can take place via a vibrationally or electronically excited molecule, or a radical created by photo dissociation. The course of the latter interaction has been studied using CO<sub>2</sub> laser pulses in the presence of SF<sub>6</sub> at normal incidence to the Si substrate. It has been suggested that gaseous or physisorbed SF<sub>6</sub> molecules are excited into higher vibrational states via coherent multiphoton excitation. In contrast to ground-state SF<sub>6</sub>, vibrationally excited SF<sub>6</sub> can dissociatively chemisorb on Si surfaces resulting to the formation of fluorine ions. Part of the chemisorbed F<sup>-</sup> ions penetrate into the Si forming a fluorosylil layer. Via a number of subsequent processes SiF<sub>4</sub> is formed and desorbs from the surface.<sup>[29][2]</sup>

With high fluences and parallel incidence of the CO<sub>2</sub> irradiation, decomposition of SF<sub>6</sub> may occur due to coherent and multiphoton absorption (via the vibrational state ladder) resulting in its dissociation.<sup>27[3]</sup> SF<sub>6</sub> molecules decompose into SF<sub>5</sub> and F atoms. SF<sub>5</sub> (being very unstable) decomposes into SF<sub>4</sub> and another F atom, which both diffuse into the Si surface and react to form SiF<sub>4</sub>. Gas-phase photodissociation of SF<sub>6</sub> producing fluorine radicals has also been demonstrated for intense femtosecond irradiation at 800 nm.<sup>[28][4]</sup>

## 2.4 Experimental Setup

Figure 2.2 shows the experimental setup. The laser beam is guided and focused inside a vacuum chamber and on top of the flat crystalline Si.

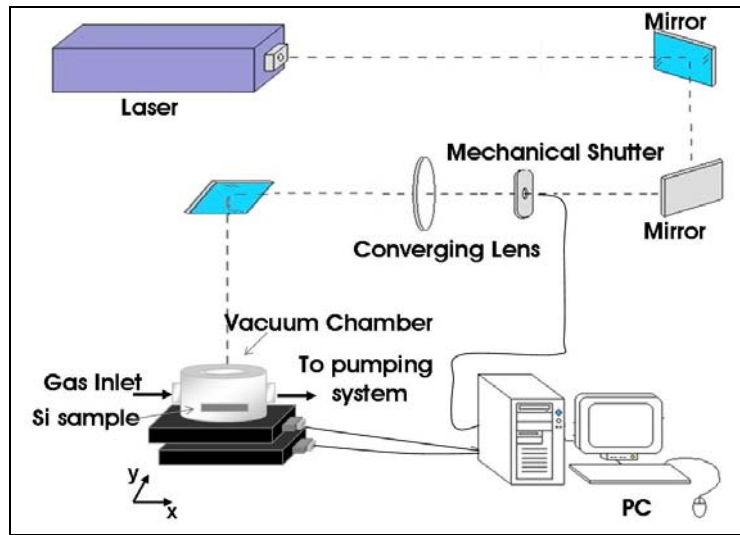


*Figure 2.2* : Experimental Setup

### 2.4.1 The Ti:Sapphire laser system

This laser system is based on a Spectra Physics Tsunami oscillator, which delivers 80-100 fs pulses at a repetition rate of 81 MHz with a power of 500 to 600 mW and a FWHM of 10 nm. The pump laser used for this system is a Spectra Physics Millennia Nd:YLF, which pumps the oscillator with a power of 5 W. A Thales Laser System (stretcher, amplifier, compressor) amplifies the beam by using another Ti:Sapphire crystal and a 12 W Q-switched Nd:YLF pump laser (B. M. Industries). During the chirped pulse amplification the repetition frequency is lowered from 81 MHz to 1 kHz by a pulse picker (pockels cell) inside the cavity of the amplifier. After being amplified the pulse is linearly polarized, it has a length of 180 fs with a repetition rate of 1 kHz and a power of 500 to 600 mW, respectively.

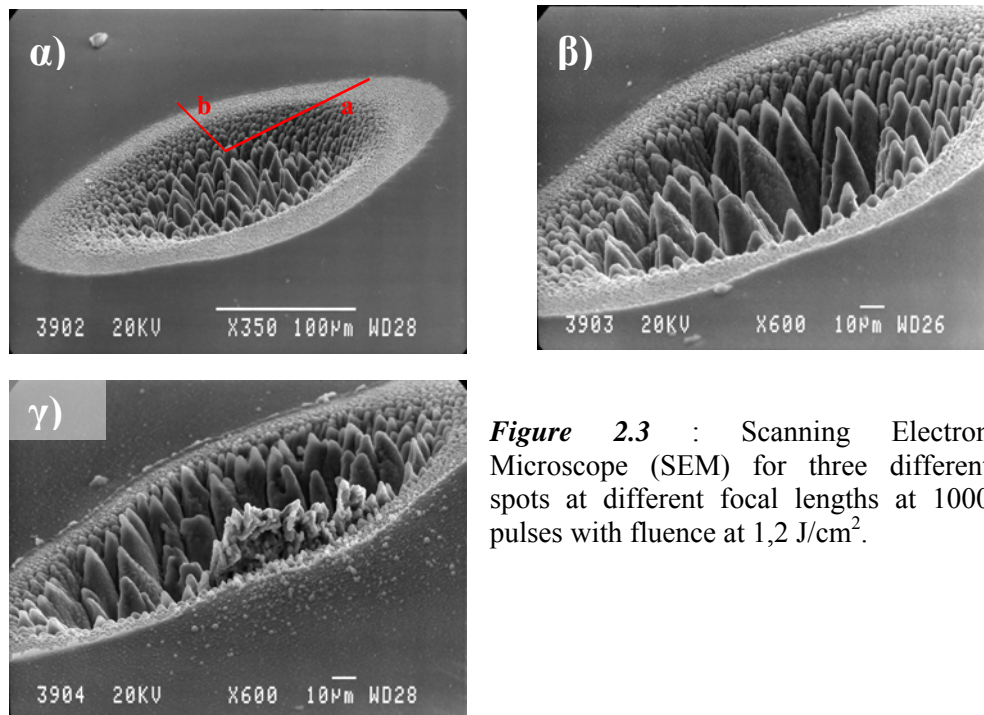


**Figure 2.3** : Scanning Electron Microscope (SEM) for three different spots at different focal lengths at 1000 pulses with fluence at  $1,2 \text{ J/cm}^2$ .

The processing chamber was placed on a computer driven high precision X-Y translation stage (Standa) with spatial resolution of  $1 \mu\text{m}$  allowing sample displacement with regard to the laser beam up to 100 mm. This system allowed control over the amount of overlap between consecutive scans when large area microstructuring was required. For this laser system operating at a repetition rate of 1 kHz, direct triggering from the laser was not possible, and so a mechanical shutter (Uniblitz) was synchronized to the computer driven translation stages, allowing direct laser pulse packages into the processing chamber.

**Figure 2.3** Shows an image from the Scanning Electron Microscope (SEM<sup>1</sup>) of a spot irradiated at 1000 pulses for three different focus distances at a fluence of  $1,2 \text{ J/cm}^2$ .

<sup>1</sup> The SEM is an instrument that produces a largely magnified image by using electrons instead of light to form an image. A beam of electrons is produced at the top of the microscope by an electron gun. The electron beam follows a vertical path through the microscope, which is held within a vacuum. The beam travels through electromagnetic fields and lenses, which focus the beam down toward the sample. Once the beam hits the sample, electrons and X-rays are ejected from the sample. Detectors collect these X-rays, backscattered electrons, and secondary electrons and convert them into a signal that is sent to a screen similar to a television screen. This produces the final image.

### **2.4.2 Development of the Si spikes with the number of pulses**

The cone-shaped structures are developed after a few hundreds of pulses. Keeping the laser fluence constant at  $1,2 \text{ J/cm}^2$  and the chamber filled with  $\text{SF}_6$  gas at 500 Torr, we irradiated the Si changing only the number of pulses. In **figure 2.4** we show a) a silicon area after 5 pulses, where a small roughness is induced, and a first indication of structures is observed and after b,c) 50 pulses. For 100 laser pulses formation of conical structures is observed. Above 1000 pulses a crater is formed in the middle of the spot with conical structures surrounding it with decreasing height from the center to the edges.

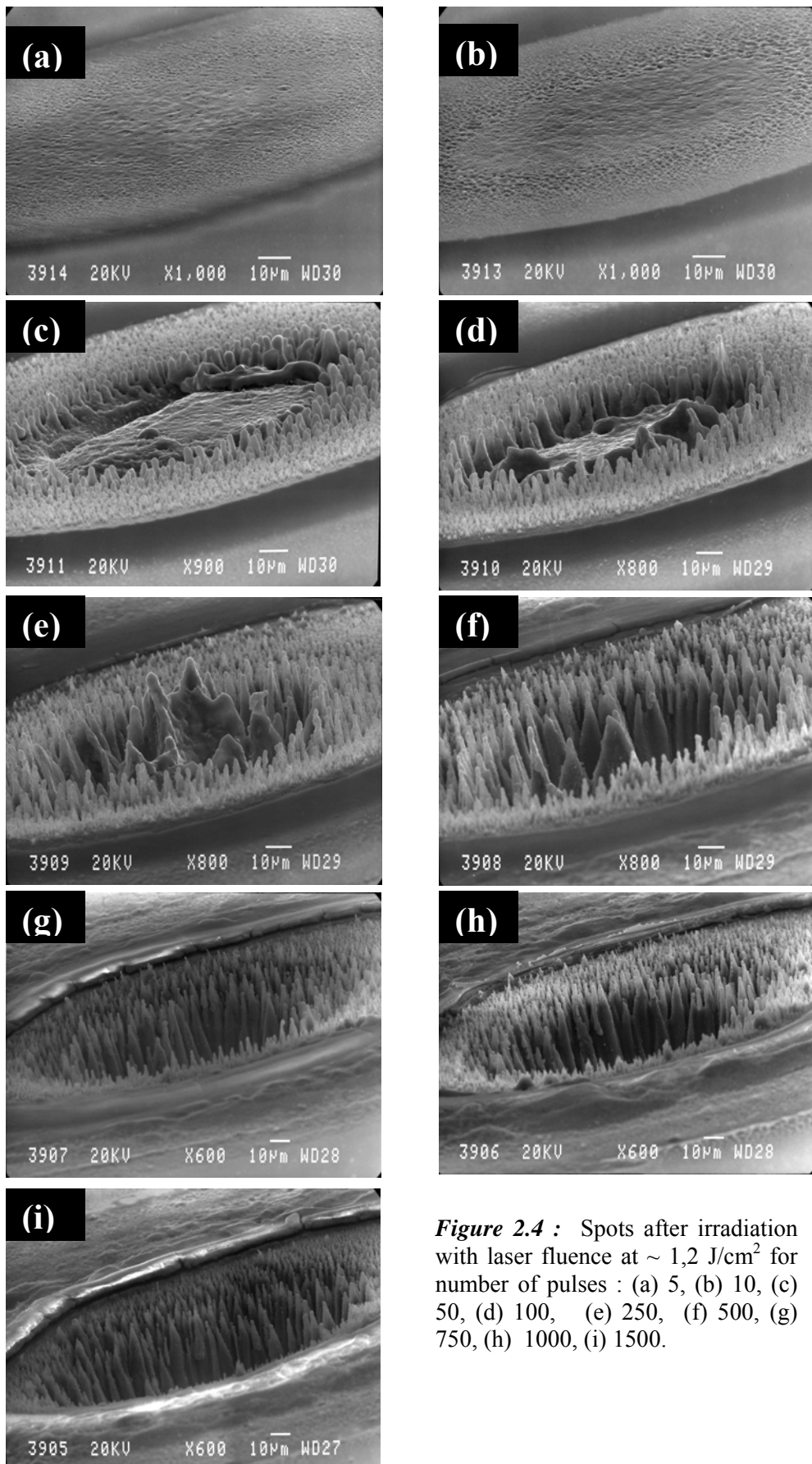


**Figure 2.4 :** Spots after irradiation with laser fluence at  $\sim 1,2 \text{ J/cm}^2$  for number of pulses : (a) 5, (b) 10, (c) 50, (d) 100, (e) 250, (f) 500, (g) 750, (h) 1000, (i) 1500.

## 2.5 Fabrication of spikes under SF<sub>6</sub> (500 Torr)

In this section we study the formation of microstructures on the surface of Si, using the Ti:Sapphire laser system ( $\lambda=800$  nm,  $\tau=180$  fs), operating at a repetition rate of 1 kHz. The effect of the laser processing parameters is investigated with a constant value of reactive gas (SF<sub>6</sub>) at 500 Torr pressure on the morphology and geometrical characteristics of the structures fabricated. For these experiments, a number of 500 pulses, were tested for fluences varying from 0.33 to 2.25 J/cm<sup>2</sup>.

The density of the spikes decreases with increasing laser fluence starting from 12x10<sup>6</sup>/cm<sup>2</sup> and reaches a plateau at 1x10<sup>6</sup>/cm<sup>2</sup>, contrarily to the height of the spikes which increases from 1.8  $\mu\text{m}$  and reaches 17 $\mu\text{m}$ , meaning bigger structures with increasing laser fluence. (**Figure 2.5(b)**). For laser fluences of 0.33 J/cm<sup>2</sup> and above we have the formation of conical structures (**Figure 2.6(a),(c),(e)**) and with increasing fluence we can observe a secondary scale roughness due to the melting and resolidification (**Figure 2.6(g),(i)**). A top view of the spikes can also be observed in **figures 2.6(b),(d),(f),(h),(j)**

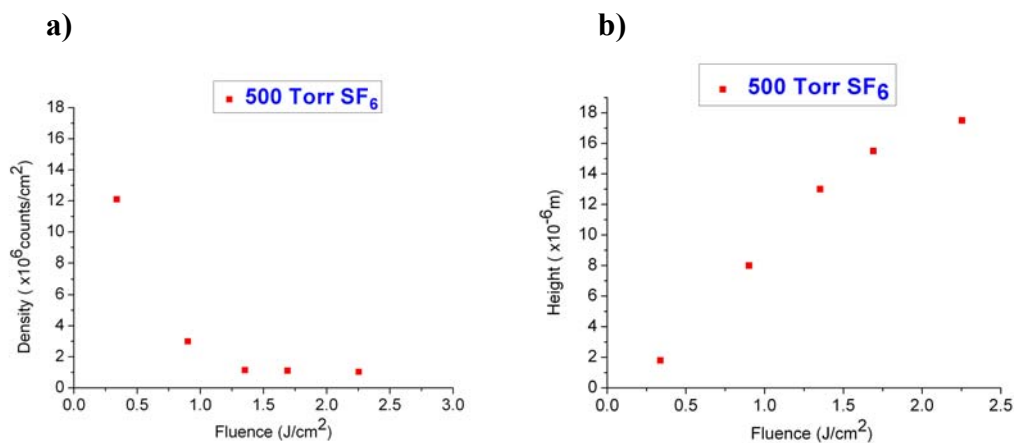


**Figure 2.5** : Morphological characteristics of the spikes fabricated using the fs Ti:Sapph laser source in a 500 Torr SF<sub>6</sub> atmosphere. Graph of the a) density and b) height as a function of fluence for the spikes at 500 Torr SF<sub>6</sub>.

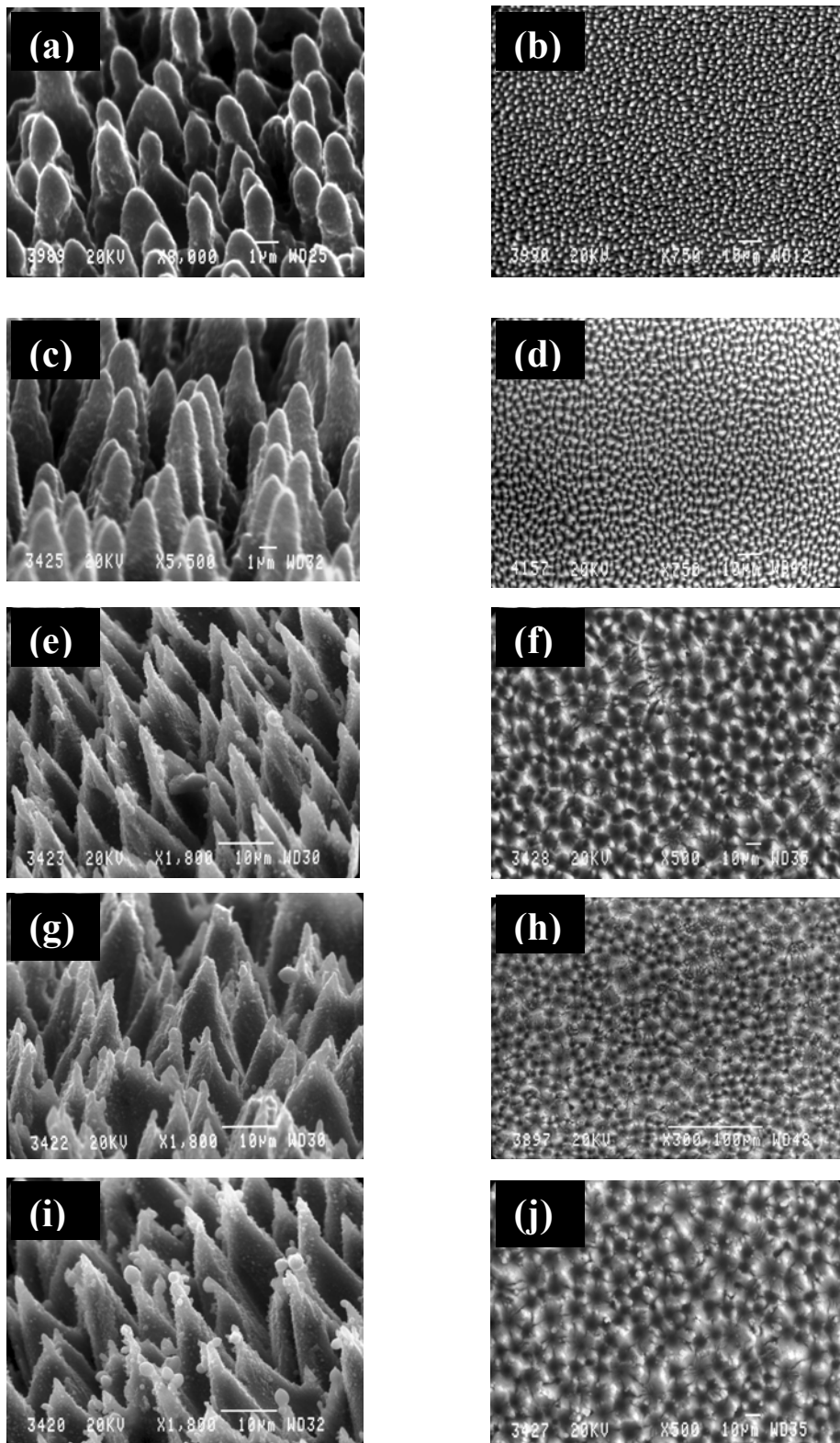


**Figure 2.6 :** Side SEM images of Si microstructures fabricated using the Ti:Sapphire laser source in the presence of 500 Torr SF<sub>6</sub> for different laser fluences. a,b) for 0.33 J/cm<sup>2</sup>, c,d) for 0.90 J/cm<sup>2</sup>, e,f) for 1.35 J/cm<sup>2</sup>, g,h) for 1.69 J/cm<sup>2</sup> for i,j) γα 2.25 J/cm<sup>2</sup>.

## **2.6 Conclusion**

As described in the present chapter laser ablation of Si with femtosecond laser pulses, in the presents of 500 Torr SF<sub>6</sub> gas, results in the formation of semi-periodical conical microstructures on its surface. Conical structures of different heights and densities were fabricated upon varying the laser fluence at the range of ( 0.34 – 2.25 J/cm<sup>2</sup>). It is shown that, contrarily to their height, the density of the spikes decreases with increasing laser fluence.

# Chapter 3

## *Theory of wettability*

### 3.1 Introduction

Control over the wettability of solids and manufacturing of functional surfaces with special hydrophobic and self cleaning properties has aroused great interest because of its significance for a vast range of applications in daily life, industry and agriculture. Superhydrophobicity is currently the focus of considerable research for a wide range of applications, such as self-cleaning surfaces, biological scaffolds, microfluidics, lab-on-chip devices, coatings for automotive and aerospace vehicles, textiles. Nature has illustrated a wide variety of superhydrophobic surfaces. Insects like Cicada orni [108] and Rhinotermitidae [109] and plants such as the sacred lotus (*Nelumbo Nucifera*) [104] exhibit unique wetting properties. In fact the lotus leaf surface has been considered as a “model” superhydrophobic, water repellent surface. The properties of the lotus leaf have been ascribed to the complex morphology present on its surface, consisting of hierarchical structuring, at two different lengthscales (see Chapter 6.4). As a consequence, the main strategy for the fabrication of any artificial superhydrophobic and water-repellent surface has been to mimic its surface topology. Simplified schemes of micro-nanomanufacturing, enabling the reproducible creation of such complex surface topologies with different lengthscales are therefore very desirable.

Several different physical and chemical patterning approaches have been employed for structuring surfaces, so as to tailor their wettability, including photolithography [110] templated electrochemical deposition [111] plasma treatments [112]. Microstructuring by lasers in specific ambient environments is particularly attractive, because it may result into structuring of solid substrates at two length scales through a simple one-step production, without a clean room facility and high-vacuum equipment requirements. The resulting surface in Si [??] consists of self-organized conical spike forests with characteristic size from a few to tens of  $\mu\text{m}$ , decorated by fine features between tens and a few hundreds of nm. Among the advantages of this technique, is that it can be applied in a wide range of materials, such as polymers [??] ceramics [??], or metals [??] in order to control surface topology, and thus open the way to controlling their wettability.

In this chapter we will study the Fundamental theory of water repellency, by defining the contact angle, the Cassie-Baxter and wenzel models and the sliding and motion of a water drop on a tilted plane.

### 3.2 Contact Angle

When small water drop is deposited on a plane surface its shape is defined by the volume of the liquid, and the surface tensions between the solid liquid and air interface. The static contact angle is strongly defined by the morphology of the surface. If the surface is ideal, meaning plane and homogeneous then the contact angle is defined as the angle at which a liquid-gas interface meets the solid surface is called the equilibrium or Young contact angle ( $\theta_0$ ) and for this, the energy of the system reaches a local minimum. [117,118,119] Gravitational forces don't play a roll here as long as the water drop is between 1-5  $\mu\text{l}$ , and the shape of the water drop is approximately a sphere.

The force balance leads to the well-known Young equation:

$$\gamma|_{lv} \cos \theta_Y = \gamma|_{sv} - \gamma|_{sl} \Leftrightarrow$$

$$\cos \theta_Y = \frac{\gamma|_{sv} - \gamma|_{sl}}{\gamma|_{lv}} \quad (\text{Eq. 3.1})$$

, where the subscripts (sg), (sl), and (lg) refer to solid-gas, solid-liquid, and liquid gas interfaces respectively (**Figure 3.1**)

The contact angle is a measure of the wetting behavior of a given surface and depending on its value a surface can be characterized as hydrophilic ( $<90^\circ$ ) (**Figure 3.1(a)**) hydrophobic ( $>90^\circ$ ) (**Figure 3.1 (b)**), or superhydrophobic ( $>150^\circ$ )

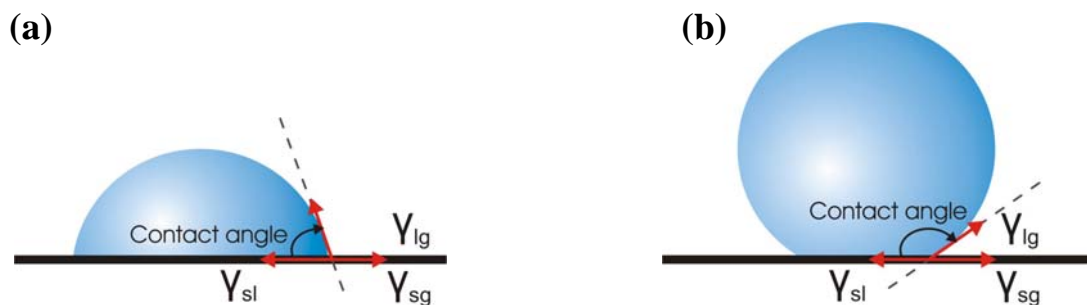


**Figure 3.1** : Contact angle for two different cases, a) Hydrophilic και b) Hydrophobic surfaces

The surface tension  $\gamma$  is a manifestation of the intermolecular forces at a surface (or interface), of a liquid on a surface, and is defined as the energy (W) needed to increase the surface area per increase in surface area (A):

$$\gamma = \frac{dW}{dA} \quad (\text{Eq. 3.2})$$

Surface tension has dimensions of force per unit length (N/m), or of energy per unit area (J/m<sup>2</sup>). According to Young's equation the higher the surface tension of a liquid on a surface, the higher the contact angle.

### 3.3 Wettability and Surface roughness: Wenzel and Cassie-Baxter states

The effect of the macroscopic surface roughness on the wettability of surfaces has been theoretically approached by two different models. In the Wenzel model [120], the liquid is assumed to completely penetrate within the entire rough surface, described as "homogeneous wetting regime" without leaving any air pockets underneath it (**Figure 3.2 (a)**). The apparent contact angle,  $\theta_w$ , is then given by the following equation:

$$\cos\theta_w = r \cos\theta_o, \quad (\text{Eq. 3.3})$$

where  $r$  is the ratio of the unfolded surface to the apparent area of contact under the droplet, and  $\theta_o$  is the contact angle on a flat surface of the same nature as the rough. Since  $r$  is always greater than unity, this model predicts that the contact angle will decrease / increase with surface roughness for an initially hydrophilic ( $\theta_o < 90^\circ$ ) / hydrophobic ( $\theta_o > 90^\circ$ ) surface.

In contrast, Cassie and Baxter (CB) (**Figure 3.2(b)**) assumed [??] that the liquid does not completely permeate the rough surface because air gets trapped underneath it. As a result a droplet will form a composite solid-liquid / air-liquid interface with the sample in contact. In this case, the apparent contact angle,  $\theta_{CB}$ , is an average of the flat surface,  $\theta_o$ , and the value for full hover over the flat surface (that is,  $180^\circ$ ) and is given by:

$$\cos\theta_{CB} = -1 + f + r_f f \cos\theta_o \quad (\text{Eq. 3.4})$$

, where  $f$  defines the fraction of the projected solid surface that is wet by the liquid and  $r_f$  is the roughness ratio of the wet area.

As  $f$  is always lower than unity, this model always predicts enhancement of hydrophobicity, independently of the value of the initial contact angle  $\theta_o$ . The lower the value

of  $f$ , the higher the contact angle measured. In contrast, when  $f=1$  and  $r_f=r$ , Equation (3.4) turns into the Wenzel equation.



**Figure 3.2 :** The two different wetting models. (a) Wenzel model, (b) Cassie-Baxter Model

Assessment of the preferred state of the droplet in contact with a rough surface is not always a trivial task. On the other hand, the apparent contact angle of a drop in contact with a structured surface, is a result of surface energy minimization of the drop. It has been found [??] that the most energetically favourable state will be the CB one when the contact angle of the flat surface,  $\theta_o$ , is less than a critical value  $\theta_c$  determined by:

$$\cos \theta_c = \frac{f-1}{r-f} \quad (\text{Eq.3.5})$$

Equation 3 is deduced by equating  $\theta_w$  of Eq.(1) with  $\theta_{CB}$  of Eq.(2) When  $\theta_o > \theta_c$ , then complete or partial wetting occurs as a result of the liquid penetration into the rough solid surface.

### 3.4 Droplet motion on superhydrophobic surfaces

It is interesting to examine the motion of a water drop when placed on a tilted hydrophobic surface. In this case the drop is shown to roll over the surface like a solid sphere, instead of sliding (**Figure 3.3**). The maximum speed obtained is limited by the viscosity of the drop which leads to a paradox, with the smaller drops moving faster than the larger ones. However one should not connect classical mechanics of solids with that of the drop's motion. While slipping every molecule of the drop is able to move to one direction of movement. In fact, it is known that the flow of liquid on the solid-liquid interface is zero, like in the case of a river. This means that the water is not slipping but rolling due to different conditions formed on the front and back contact of the water drop with the surface. Continuing this creates a circular flow inside the drop, making it move. For this the slipping and rolling of water drops are fundamentally different.

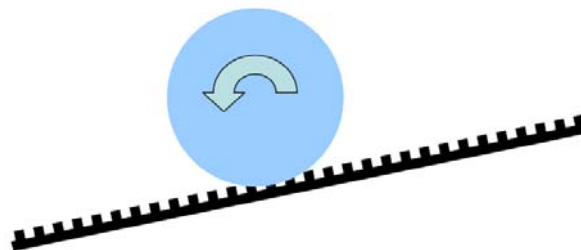


*Figure 3.3* : Droplet motion on a rough surface. the water is not slipping but rolling

### 3.4 Restitution Coefficient

Plants and creatures have evolved outer layers that are hydrophobic, which protects the leaves from being saturated with water in the form of rain or dew. For example, the lotus has an extremely rough surface with a waxy coating. Rain drops are repelled off the leaf, literally bouncing off when they strike the surface. On the other hand, birds and butterflies have evolved so they can still fly in the presence of rain drops in the air.

The behavior of an impinging water droplet on different substrates proves to be an important aspect in the environment and everyday life. Depending on the surface, and most importantly, the energy of the droplet, the drops will react differently when contacting the solid surface. As a water droplet hits a solid surface, the initial spherical shaped droplet is forced into a pancake-like form that stretches out over the surface. The kinetic energy of the droplet forces it to spread over the surface of the solid. If the surface is hydrophilic, the liquid

will continue to spread with minimal retraction. However, if the surface is hydrophobic, the liquid and surface are repulsive. The drop retracts from this pancake-like shape to a spherical shape. If this retraction is violent, the drop repels off the surface, in what we call bouncing.

By keeping other variables constant in the experiment, such as the hydrophobic surface, the liquid, and the size of droplet, the different properties of droplet bouncing can be compared. When increasing the height from which the droplet falls, the drop's fall velocity and kinetic energy are, in turn, increased. The Weber number is defined as the ratio of the drop's kinetic energy to surface energy:

$$We = \frac{\rho V^2 r}{\gamma} \quad (\text{Eq. 3.6})$$

, where  $\rho$  is the density of water ( $1000 \text{ kgm}^{-3}$ ),  $V$  is the velocity of the droplet before respect to air ( $0.07275 \text{ kgs}^{-2}$ ). This number is dimensionless since

$$[We] = [\text{kgm}^{-3}][\text{m}^2\text{s}^{-2}][\text{m}][\text{kg}^{-1}\text{s}^2]. \quad (\text{Eq. 3.7})$$

Another representation of kinetic energy, and specifically loss of kinetic energy, is shown in the restitution coefficient (RC). The RC is defined as the ratio of before and after velocities of an impact on the surface [5]. It is represented as:

$$RC = \frac{V_f}{V_i} \quad (\text{Eq 3.7})$$

or

$$RC = \sqrt{\frac{h}{H}} \quad (\text{Eq 3.8})$$

where  $V_f$  is the droplets velocity after impact,  $V_i$  is the velocity before impact,  $h$  is height to which droplet bounces, and  $H$  is the height from which the droplet falls. The initial RC of a droplet refers to the droplets first bounce off the surface, although a RC can be calculated for each consecutive bounce. The RC ranges in values between 0 and 1, where a value of zero implies no bounce occurred after contact with the surface and a value of one means a complete and perfectly elastic bounce occurred,  $V_f = V_i$ .

# Chapter 4

## *Tailoring the wetting response of silicon surfaces*

### 4.1 Introduction

In this chapter we will investigate the wetting properties of the silicon structured surfaces studied in chapter 2. Based on the different morphologies obtained due to the variation of the laser fluence, we will study its impact on the wetting properties having in mind the theory discussed in chapter 3. The study will be first made on the Si structured surfaces, and second on the same surfaces covered with a hydrophobic organosilane monolayer. The determination of hydrophilicity / hydrophobicity will be made depositing a water drop and measuring the static **contact angle (CA)**.

### 4.2 Static CA measurement

Static contact angles were measured with an automated tension meter using the sessile drop method. The Si structured surface with the water drop on it is placed inside a cell surrounded by water to keep a level of humidity. An optical fiber illuminates the water drop and a CCD camera records the drop's image on a computer (**Figure 1**). Finally a complex mathematical algorithm taking in account the surface tension of the water drop, the gravitational force and the density calculates the value of the CA.

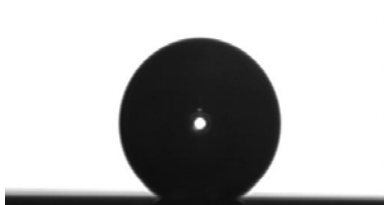


**Figure 4.1:** Image of a 2 $\mu$ l water drop sitting on a Si structured surface captured by a CCD camera from a tensionmeter.

### 4.3 Morphology and Static CA Measurements

In this part of our work we study the effect of different surface morphologies on the wettability of processed Si. Textured Si surfaces have been fabricated by employing the same number of laser pulses (an average of 500) at different fluences (**Figure 4.2**). Increasing the incident energy per unit area causes remarkable changes in the structures shape, dimension and density. At low irradiation fluences laser heating induces melting of the surface producing a rippled landscape, with structures not completely physically separated (**Figure 4.2(a)**). Upon increasing the fluence (**Figure 4.2(b) and 4.2(c)**), conical microstructuring is promoted on the Si surface, with structures becoming more pronounced and spatially separated. In this regime the average spikes spacing, base diameter and height increase with laser fluence. For larger fluence values (above  $\sim 1.0 \text{ J/cm}^2$ ), the spikes growth reaches a plateau, where the base diameters stabilize around  $8 \mu\text{m}$ , while the height stabilizes around  $17 \mu\text{m}$ .

Besides directly affecting the micrometer-scale surface topology, increasing fluence is also crucial to induce a more pronounced sub-micrometer decoration on the spikes walls. In particular, the protrusions with size from tens to a few hundreds of

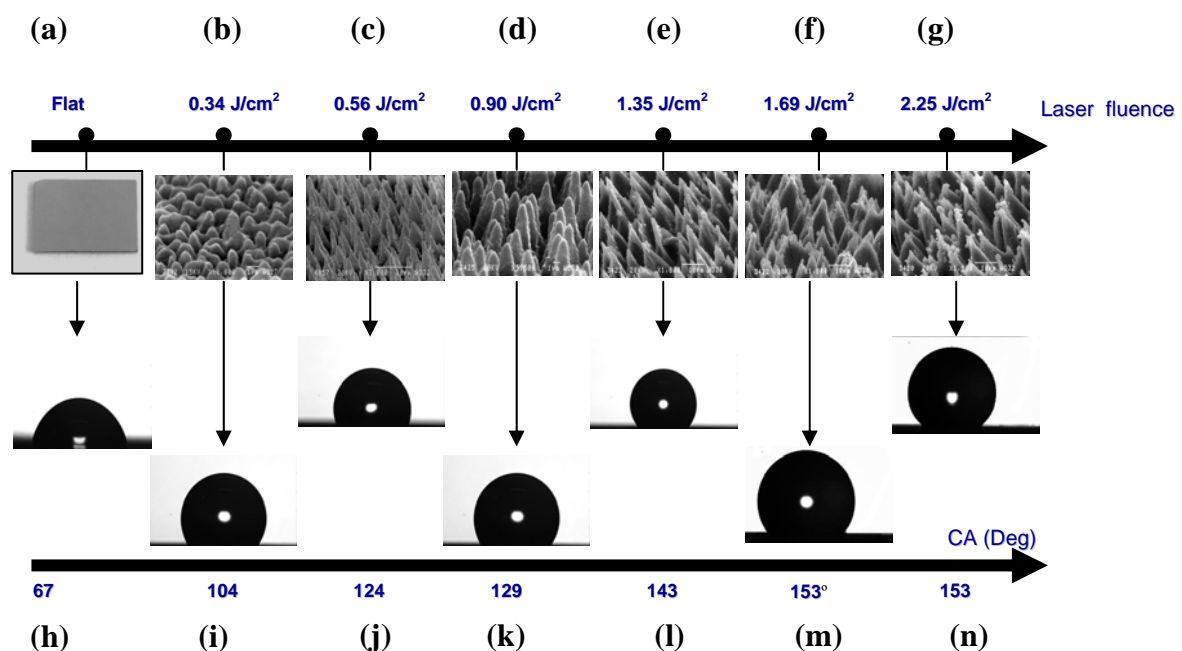


**Figure 4.2 :** (a)-(g) Side scanning electron microscope view of Si surfaces structured by fs-irradiation at different laser fluences. (h)-(n) Images of water droplets on the corresponding structured Si surfaces.

nanometers, which constitute the second length-scale pattern on the Si surface, become more evident as the laser fluence increases (**Figure 4.2(e), 4.2(f) and 4.2(g)**). The micrometer-scale conical together with the nano-scale features, generated by the surface prongs on the cones result into a significant increase of the overall roughness. Some pictures of the water drops lying on the structured Si surfaces are shown in **Figure 4.2** under the Si structured surfaces.

Changes in the observed wettability may be attributed to a synergy of surface chemistry and roughness. It is known that the formation of a native oxide layer is initiated on the Si surface immediately after the HF treatment. [124,125] Its thickness changes very slowly in the first few hours (an increase of  $\sim 2\text{\AA}$  in the first hour).[124]

Particular care was given in our experiments, in performing the CA measurements only a few minutes after the HF treatment, therefore ensuring the presence of similar native oxide thicknesses in all the samples. Based on the above findings, the structured Si surfaces are considered to maintain a similar chemical composition and the observed changes in the wettability may be attributed primarily to the morphological changes obtained at different laser fluences.

On the lower axis of **figure 4.2** we can observe the changes in the static CA of a  $2\mu\text{l}$  nanopure water drop. The CA increases rapidly even for the surfaces with low roughness starting at  $104^\circ$  structured at energies around  $0.34\text{ J/cm}^2$  (**Figure 4.2(i)**). Starting from flat Si with a CA of  $67^\circ$  we observe a gradual increase and reaches a plateau at  $153^\circ$ . Using the general Cassie – Baxter equation (Chapter 3 equation 6) one can obtain information about the wettability of the structured surface For the samples exhibiting the pronounced two-lengthscale surface roughness, namely those obtained by irradiation fluences larger than  $1.0\text{ J/cm}^2$ , the CA values reach a plateau around  $153^\circ$  (see **Figure 4.2(f),(g)**). Therefore, for these samples the liquid is in contact with a practically constant solid surface, and thus, the factors  $f$  and  $r_f$  in Eq. 3.4 remain constant. Assuming that at these irradiation regimes the formed structures roughly resemble cones (the nanometer scale formed features are integrated into the cone structure), a simple geometric equation correlates the factor  $r_f$  with the angle of the formed cones, which is evaluated by the scanning electron microscopy pictures. Finally, by Eq. 3.4 the factor  $f$  is calculated  $\sim 0.13$ . Namely, the surface of the base of the wetted Si cone is about 13% of the total base of the formed Si cones.

Besides nanopure water two other liquids with different surface tension were used namely glycerol and ethilenglycol 50%, so to study the change in the static CA. **Figure 4.3** shows a diagram for the three liquids. The first values on the diagram represent the values of the CA on the flat Si followed by the values with different surface roughness. Water which

has the highest surface tension also takes maximum values for the CA as shown before, and for glycerol and ethilenglycol values start at  $104^\circ$  and  $100^\circ$  and reach a plateau at  $121^\circ$  and  $114^\circ$  respectively.

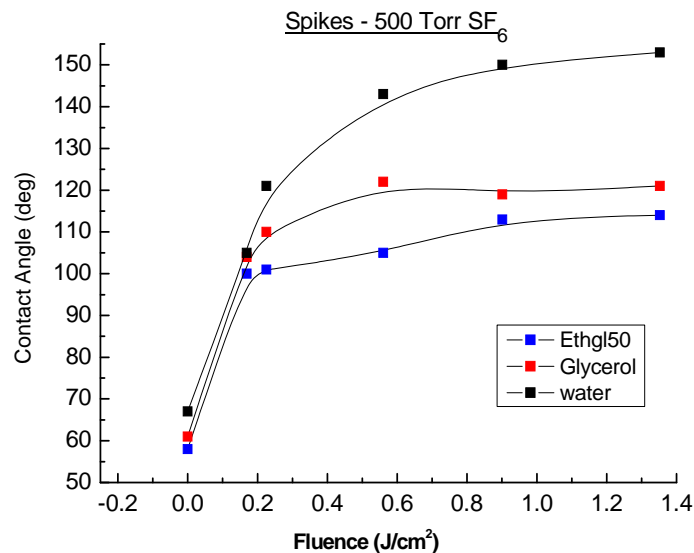


**Figure 4.3** : CA measurements for three different water drop liquids of  $2\mu\text{l}$  : nanopure water, glycerol and ethilenglycol 50%,

Previous studies in which initially hydrophilic surfaces became hydrophobic upon structuring, were based on the deposition of a hydrophobic coating on the top of the structure.[126]On the contrary, the results of this work demonstrate that a Si surface upon patterning becomes hydrophobic, without any need for coating deposition. The results of this work clearly demonstrate that Si hydrophobicity increases upon laser structuring, and this behavior can be described assuming that air pockets are trapped underneath the liquid. Eq. 3.2, which describes this behavior, can give quantitative information about the partial penetration of the water drop into the formed Si features.

#### **4.4 Dimethyldichlorosylan (DMDCS) coating, and static CA measurements**

Considering the above we are able to fabricate surfaces which CA reaches up to 153°. The question that arises is whether or not we are able to increase the CA of the surfaces fabricated at lower fluences and also if the value of 153° is the maximum that can be obtained. The answer is positive and we are able to achieve it by coating the structured surface with a hydrophobic monolayer of Dimethyldichlorosylan (CH<sub>3</sub>)<sub>2</sub>SiCl<sub>2</sub> (DMDCS), which can assemble into high quality conformal coatings on flat Si surfaces [48] resulting in a material with a low surface energy that can maintain its hydrophobic properties for long periods of time and for a wide temperature range. The samples were placed in a flask containing 0.5 ml of DMDCS reagent where hydrophobic DMDCS monolayers were deposited on their surface via adsorption reactions. The silanization process employed is similar to that reported in the literature [50]. After 12 hours the sample was removed from the flask and washed with με 2/3 Toluene, 3/3 Ethanol, 1/1 Ethanol/Water, 2/3 Water, 2/3 Ethanol, 3/3 Water. Finally the sample was annealed at 120° C for 30 minutes. The thickness of the layer was measured to be 3-4 nm. **Figure 4.4** shows an Atomic force image (AFM) of a structured surface before and after silanization. We can observe that the roughness after the silanization process hasn't changed significantly and the thickness is less than 4nm.

As we can observe from the charts in **Figure 4.5** after the DMDCS coating, a great increase in the CA can be observed for a 2μl nanopure water, glycerol and ethyl/glycol drop. As can be clearly seen CA for the flat silicon starts now at 104° and for the structured Si at low fluence it takes a value of 140° reaching a maximum value of 163°. This means an overall of 10° - 30° increase of the static CA for water. Similar for glycerol and ethyl/glycol a 35° increase can also be observed.

In addition for nanopure water the structured surfaces have a very low sliding angle of only 5°, making the water drop able to slide very easily across the surface with only a small tilt.

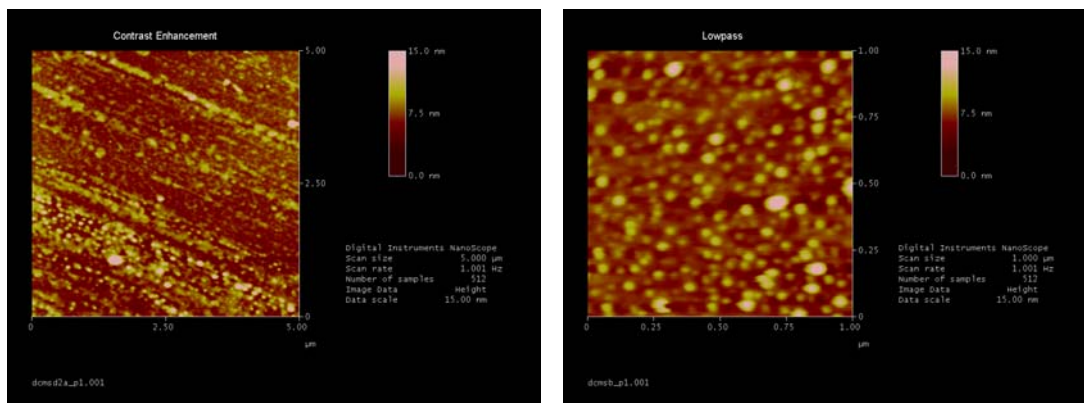


Figure 4.4 : Atomic Force microscopy images (AFM) were we can observe the morphology of the Si structured surface after the DMDCS coating with thickness 3-4 nm

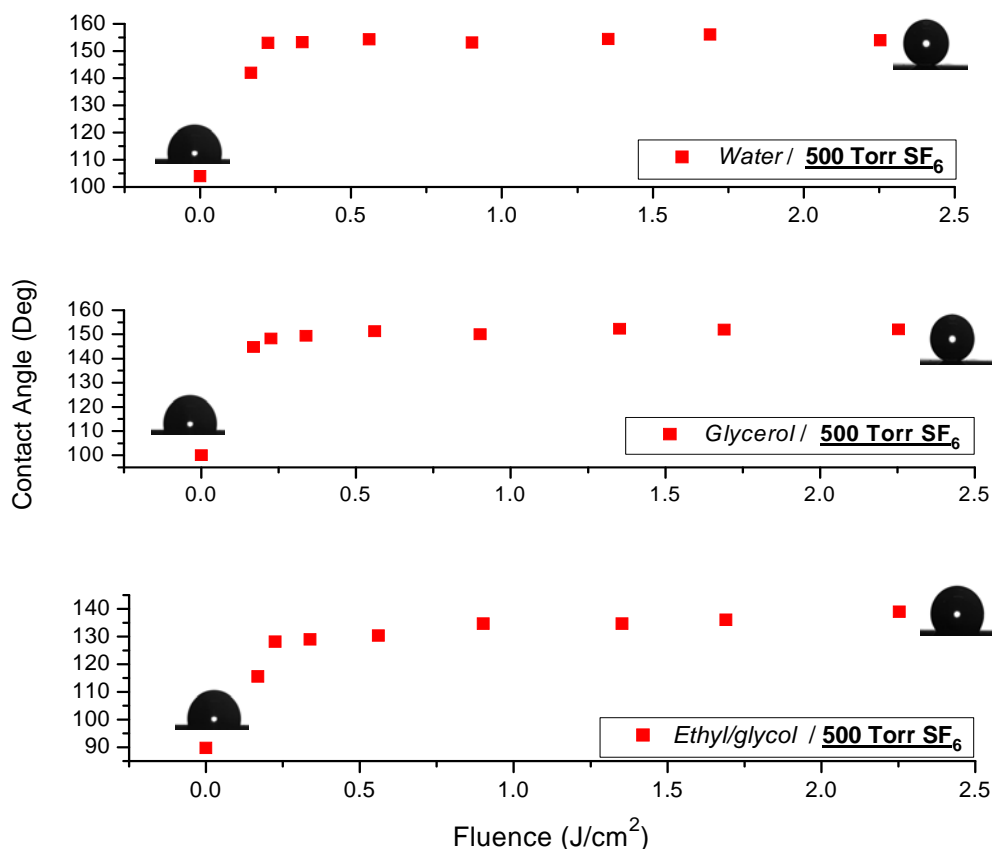
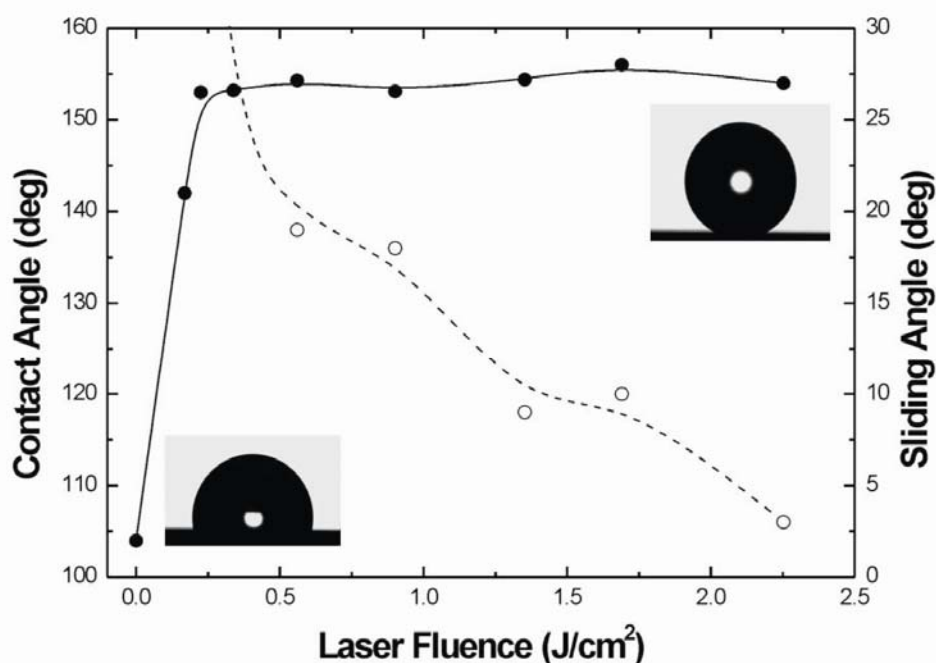


Figure 4.5 :\_CA increase of a 2µl nanopure water, glycerol and ethyl/glycol drop on a Si structured surface after DMDCS coating

## 4.5 Sliding Angle Experiments

As a rule, superhydrophobic surfaces should exhibit both high contact angle and little or no hysteresis. Hysteresis denotes the deviation between the advancing and receding contact angles of the drop due to pinning of the contact line on surface defects, and results in an increase of the inclination required for the droplet to slide along the surface. On the superhydrophobic lotus leaf, a tilt of only  $3^\circ$  is sufficient to initiate droplet motion. **Figure 4.6** shows the sliding angles of the laser structured surfaces, as a function of laser fluence (also summarized in **Table 1**). Water droplets leave the structured area at tilt angles lower than  $10^\circ$  for samples treated at fluences higher than  $\sim 1.5 \text{ J/cm}^2$ . Interestingly, these high-fluence samples exhibit the most pronounced second length-scale surface roughness. Samples in the mid fluence range ( $0.7 - 1.5 \text{ J/cm}^2$ ) do not meet the criteria for superhydrophobicity; they exhibit high sliding angles although they show similar contact angle to their high-fluence counterparts. At fluences lower than  $0.7 \text{ J/cm}^2$ , water drops remain pinned on these surfaces, at the highest sliding angles utilised.



**Figure 4.6** : Static contact angle (●) and sliding angle (°) measurements of a water drop on structured Si surfaces plotted as a function of laser fluence. For fluences below  $0.5 \text{ J/cm}^2$  the sliding angles are higher than the  $30^\circ$  limit of our measurement setup. The lines are guides for the eye. Images of the droplet on the flat as well as on the structured Si surface are shown at the insets.

motion on a surface is considered. Motion initiation, at very low inclination angles ( $5^\circ$ ) on the high-fluence superhydrophobic surfaces, is translated into a small gravitational force required

to initiate motion. In other words the friction between the droplet and structured surface is accordingly low. Low frictional motion is a key feature behind the unique lotus self-cleaning property and it is therefore desirable in any corresponding application, as it provides for efficient removal of dirt particles even when long travel distances are necessary.

Controllable manipulation of liquids has been the subject of considerable amount of scientific research for the development of micro-fluidics and lab-on-chip devices. In search of ways to efficiently drive a drop to specific sites in order to perform discrete functions such as mixing, analysis, reaction and storage, different approaches have been implemented, including thermal [i], chemical [ii], electrochemical [iii] and light-driven methods [iv]. The possibility of selective laser structuring may give the ability to drive a drop under gravity along a patterned line and deliver it to a specific location where it can be immobilized and perform a desired operation; even though the water drop is highly mobile on the patterned areas (**Figure 4.6**) it shows high contact angle hysteresis on the flat regions of the sample. **Figure 4.7** shows the initial stages of the motion of a 4 $\mu$ l droplet close to the structured-unstructured area interface, upon the action of a gravitational force imposed by slightly tilting the sample (5°), in the case of a sample irradiated at the highest laser fluence. The drop starts slipping along the superhydrophobic surface (**Figure. 4.7 (a)-(d)**), with a center of mass velocity of ~0.3 cm/s. The gravitational force required to initiate this motion is calculated to be 3.4  $\mu$ N. When the advancing front of the drop reaches the interface (**Figure. 4.7(d)**) it experiences a surface tension gradient (a result of surface morphology gradient) which forces it to escape the superhydrophobic surface and land on the flat region of the sample on which it is thereafter immobilized (**Figure 4.7 (e)**).

Assessment of the preferred state of the droplet in contact with a rough surface is not always a trivial task. On the other hand, the apparent contact angle of a drop in contact with a structured surface, is a result of surface energy minimization of the drop. It has been found [v] that the most energetically favourable state will be the CB one when the contact angle of the flat surface,  $\theta_o$ , is less than a critical value  $\theta_c$  determined by:

$$\cos \theta_c = \frac{f-1}{r-f}, \quad (\text{Eq 4.1})$$

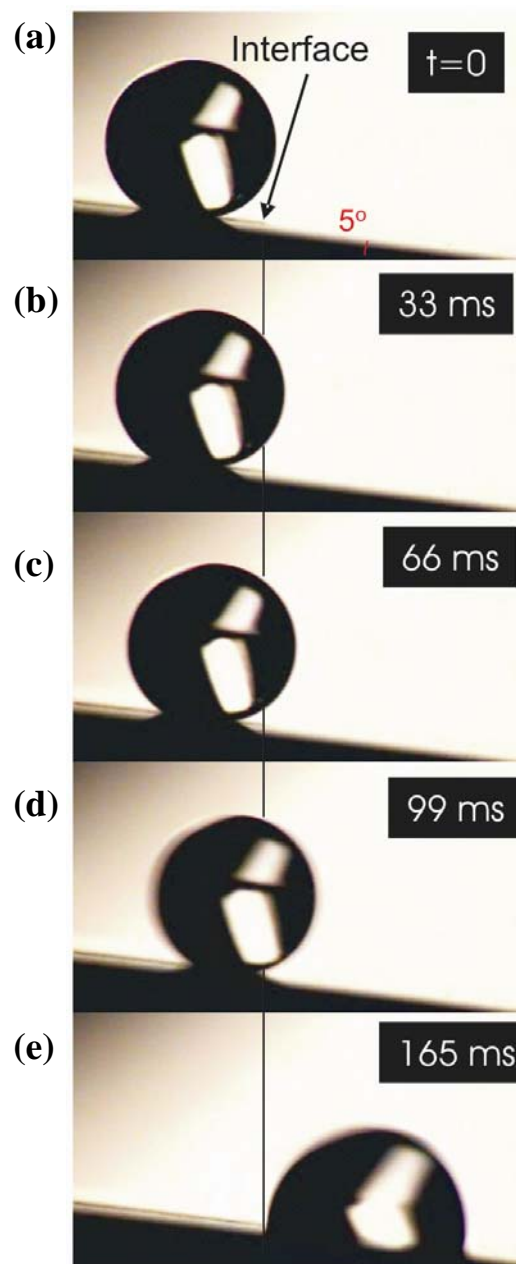


**Figure 4.7 :** (a)-(d); Snapshots of a 4 $\mu$ l water drop moving along on a 5° tilted superhydrophobic surface under the action of a gravitational component parallel to a superhydrophobic surface, as its advancing edge approaches the interface with the unstructured material. After this point (e) the drop experiences a surface tension gradient, imposed by the morphology change, forcing it to land on the unstructured part of the sample. The drop will thereafter stay pinned on that location independently of the sample inclination.

When  $\theta_o > \theta_c$ , then complete or partial wetting occurs as a result of the liquid penetration into the rough solid surface.

Contact angle hysteresis at the two states can be very different [vi]; while it is extremely small in the CB state, it takes very large values in the Wenzel state. Accordingly a much smaller sliding angle is expected for the CB state when compared to the Wenzel. Hysteresis originates at the defects of the solid surface, whereby pinning of the liquid occurs. In the Wenzel state the number of such defects is high due to extended solid-liquid contact area. The opposite effect is observed in the CB state in which the droplet effectively sits on air. A Wenzel droplet is thus much more adhesive than a CB one, even when it exhibits a high contact angle. For the fabrication of superhydrophobic surfaces it is important to design textures for which the CB state is energetically more favourable than the Wenzel state.

Assuming that the Si structures formed roughly resemble truncated cones, the factors  $r$  and  $f$  can be deduced, for each sample, from the geometrical parameters obtained by image processing of the corresponding SEM pictures. The critical angle  $\theta_c$  can then be calculated from **Equation 4.1** and is listed in **Table 1**. Since the equilibrium contact angle of the flat Si silanized surface is  $\theta_o = 104^\circ$ , we observe that the above criterion  $\theta_o < \theta_c$  is fulfilled only for the samples patterned at high laser fluences. Therefore the Cassie-Baxter state should be favoured in those fluences. This is also consistent with the sliding angle results, indicating that superhydrophobicity and low frictional motion is always in accordance with a stable Cassie-Baxter state. On the other hand the preferred state of the low- fluence samples is the Wenzel one, which can explain their inferior wetting response.

Sample	Laser fluence ( $J/cm^2$ )	Cone density ( $cm^{-2}$ )	$r$	$f$	Experimental results		$\theta_c$ (deg)	Stable state
					CA (deg)	SA (deg)		
SP1	0.37	$5.2 \times 10^7$	2.71	0.10	142	> 30	110	W
SP2	0.45	$2.2 \times 10^7$	2.56	0.09	153	> 30	112	W
SP3	0.56	$1.2 \times 10^7$	3.40	0.05	153	> 30	109	W
SP4	0.78	$4.0 \times 10^6$	1.86	0.10	154	19	121	W
SP5	1.13	$1.5 \times 10^6$	1.32	0.20	153	18	135	W
SP6	1.56	$1.5 \times 10^6$	3.95	0.02	154	9	104	CB
SP7	1.91	$1.5 \times 10^6$	4.30	0.03	156	10	103	CB
SP8	2.30	$1.5 \times 10^6$	5.30	0.04	154	3	100	CB

**Table 1:** Morphological and wetting parameters of the laser structured Si samples prepared at various laser fluences. For each sample, the cone density, solid fraction  $f$ , roughness factor  $r$ , contact angle (CA) and sliding angle (SA) are shown (see text for definitions). In order to identify whether the stable state is the Cassie-Baxter (CB) or the Wenzel (W), we compare the contact angle of the flat surface ( $\theta_0=104^\circ$ ), with the critical angle,  $\theta_c$ , as defined in the text.

## **4.6 Conclusion**

In the present chapter the changes in wettability were observed after the surface structuring of Si by laser ablation. The conical microstructures created after laser ablation have a direct impact on the wettability of our structures making the hydrophobic. A 2 $\mu$ l nanopure water drop was placed gently on the Si surface and the static CA was measured. Result showed the water drops lie in the hydrophobic state taking values from 121° - 135°. An additional increase of the static CA was observed after coating the surface with a hydrophobic monolayer Dimethyldichlorosylan (DMDCS) with values reaching up to 163°. In addition the structured surfaces have a very low sliding angle of only 5°, making the water drop able to slide very easily across the surface with only a small tilt.

- 
- <sup>i</sup>. A. M. Cazabat, F. Heslot, S. M. Troian, P. Carles: *Nature* **346**, 842 (1990).
  - <sup>ii</sup>. M. K. Chaudhury, M. Whitesides: *Science* **256**, 1539 (1992).
  - <sup>iii</sup>. B. S. Gallardo, V. K. Gupta, F. D. Eagerton, L. I. Jong, V. S. Craig, R. R. Shah, N. L. Abbott: *Science* **283**, 57 (1999).
  - <sup>iv</sup>. K. Ichimura, S. K. Oh, M. Nakagawa *Science* **288**, 1624 (2000).
  - <sup>v</sup>. A. Lafuma, D. Quere: *Nature Materials*, **2**, 457 (2003).
  - <sup>vi</sup>. D. Quere, A. Lafuma, J. Bico: *Nanotechnology* **14**, 1109 (2003).

# Chapter 5

## *Mimicking Nature : Learning from the Lotus Leaf*

### 5.1 Introduction

The water repellency and self-cleaning properties of many plant surfaces have been qualitatively and sometimes quantitatively attributed to not only the chemical constituency of the cuticle covering their surface, which is composed by soluble lipids embedded in a polyester matrix, but, even more importantly, to the specially textured topography of the surface.[1–3] It is understood that the microstructured rough surface enhances the effect of surface chemistry into superhydrophobicity, reduced particle adhesion and water repellency. Actually, in the cases of the most famous water repellent plant leaves like *Nelumbo nucifera* (the sacred Lotus **Figure 5.1**) or *Colocasia esculenta*, a dual scale roughness has been



**Figure 5.1** : Nature's lotus leaf (*Nelumbo nucifera*)

observed on their surfaces created by papillose epidermal cells and an additional layer of epicuticular waxes. The roughness of the papillae leads to a reduced contact area between the surface and a liquid drop (or a particle) with droplets residing only on the tips of the epicuticular wax crystals on the top of the papillose epidermal cells. As a result, contaminating particles can be picked up by the liquid and carried away as the droplet rolls off the leaf; this was coined the “Lotus Effect” by Barthlott and Neinhuis, [1] who then organized a consortium trying to develop self-cleaning products.[4] Similar behavior has been observed on other biological surfaces like the wings of *Cicada orni* [5] or *Rhinotermitidae*[6] insects. water repellent surface exhibits certain remarkable wetting characteristics originating from very high contact angles and very small values of contact angle hysteresis (less than 5°): [7] droplets roll down these surfaces at a speed faster than that of a solid sphere rolling under gravity, [8] they can fully bounce after impacting the surface[9,10] whereas the time of contact of an impacting droplet with the surface is independent of its velocity.[10]

Water repellency was discovered very early when Boys noticed that water deposited on a lycopodium layer rolled itself up into perfect little balls. [11] However, it has attracted the interest of the scientific community over the last ten years following the observations of the microtextures of plant surfaces and the first development of super-water-repellent surfaces possessing a fractal microstructure; [12] the latter were created spontaneously when

alkylketene dimmer was solidified from the melt. Water repellency as well as the development of super-hydrophobic surfaces are currently the focus of considerable research because of a range of potential applications, such as the development of self-cleaning surfaces, microfluidics, lab-on-chip devices, low friction coatings, water proof and anti-rain textiles, etc. [13–15] The actual strategy consists in mimicking superhydrophobic biosurfaces by designing rough substrates out of hydrophobic materials. [16,17] This has been implemented in a variety of bottom-up or bottom-down approaches [18] like deposition of functionalized particles [19–22] or micelles [23] on surfaces, solvent treatment of polymer surfaces, [24] growth of aligned carbon nanotube[25–27] or ZnO nanorod films, [28] deep silicon dry etching[29] or anisotropic plasma etching (“black silicon method”) [30] as well as X-ray lithography. [31]

## 5.2 Preparation and study of the Structures

In this chapter we have prepared artificial surfaces which can quantitatively mimic both the structure and the water repellent characteristics of the natural Lotus leaf. These surfaces possess hierarchical micro- and nano-structures and are prepared with a simple one-step production process utilizing ultrafast (femtosecond) laser irradiation of a silicon surface under a reactive gas atmosphere discussed in **chapter 2**. [38,39] This leads to a surface morphology that mimics that of the sacred Lotus leaf. Silanization of the dual-scale roughened surface leads to contact angle values of  $154^{\circ} \pm 1^{\circ}$  and to very small contact angle hysteresis of  $5^{\circ} \pm 2^{\circ}$  both very similar to the values of the Lotus leaf. The water repellency of the surfaces and its relation to that of the Lotus leaf was quantified by investigating the restitution coefficient of water droplets of various sizes bouncing off the surfaces as a function of their impact velocity. It is found that these structured surfaces constitute one of the most water repellent artificial surfaces ever reported, which are as efficient as the sacred Lotus leaf. Images of a water droplet lying on the artificial surface are shown in **Figure 5.2(a), (b)**, which can be directly compared to those of a droplet lying on the surface of a natural leaf of *Nelumbo nucifera* (Lotus leaf) shown in **Figure 5.3(a), (b)**.

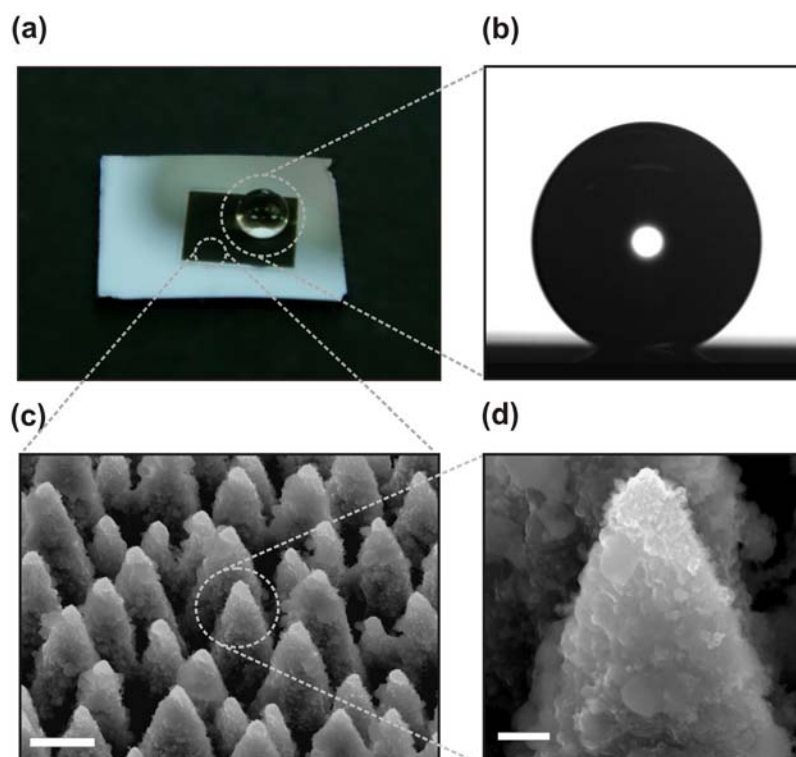


**Figure 5.2:** (a) Picture of a water droplet on the artificial structured silicon surface (dark area). (b) Static contact angle measurement of a water droplet of 0.78 mm radius on the artificial surface; the contact angle is  $154^{\circ} \pm 1^{\circ}$ . (c) SEM image of the artificial surface comprising protrusions with conical or pyramidal asperities with average sizes of  $\sim 10 \mu\text{m}$  with surface density  $1.0 \times 10^6 \text{ cm}^{-2}$  (scale bar 5 mm). (d) High magnification SEM image of a single protrusion depicting nanostructures of sizes up to few hundred nanometers on the slopes of the protrusions (scale bar 1  $\mu\text{m}$ ). The surface was structured in the presence of 500 Torr  $\text{SF}_6$  at a laser fluence of  $2.47 \text{ J/cm}^2$  with an average of 500 pulses.

The static contact angle of water on the artificial surface is measured as  $154^{\circ} \pm 1^{\circ}$  with a contact angle hysteresis of  $5^{\circ} \pm 1^{\circ}$  whereas those on the Lotus leaf as  $153^{\circ} \pm 1^{\circ}$  and  $4^{\circ} \pm 2^{\circ}$ , respectively. **Figure 5.2(c)** and **d** show scanning electron microscopy (SEM) images of the surface of the Lotus leaf, which comprises randomly distributed almost-hemispherically-topped papillae with sizes  $5\text{--}10 \mu\text{m}$  (height to basal radius aspect ratio  $\pm 1$ ) decorated with branch like protrusions with sizes of about 150 nm (**Figure 2(d)**); these observations are in agreement with earlier reports. [3,16,26] **Figure 1(c), (d)** show the SEM micrographs of the most water repellent artificial surface, which exhibits the highest contact angle and the lowest hysteresis among the different

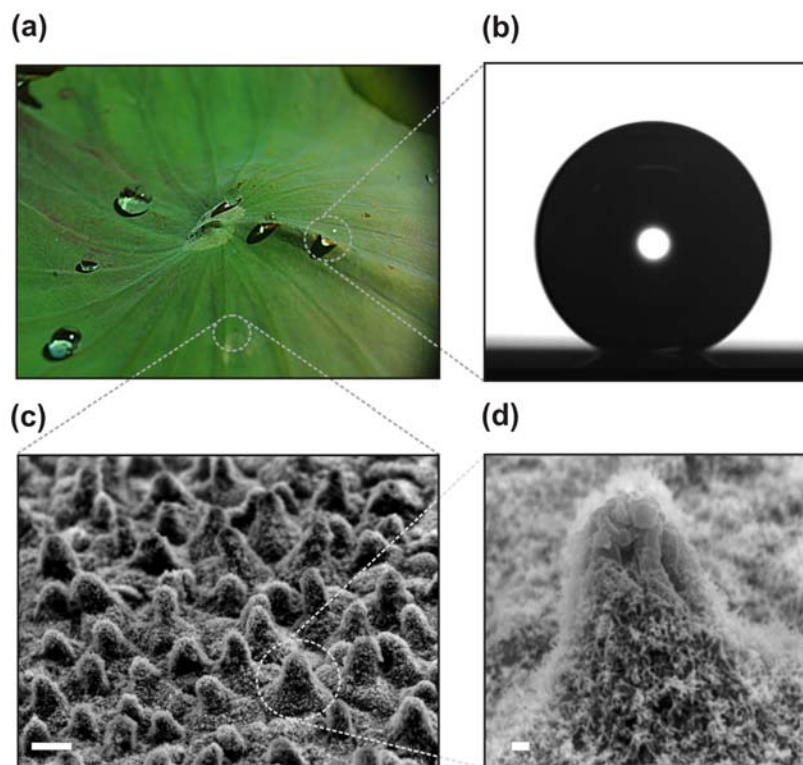


**Figure 5.3 :** (a) Picture of water droplets on a *Nelumbo nucifera* (Lotus) leaf. (b) Static contact angle measurement of a water droplet of 0.78mm radius on the Lotus leaf surface; the contact angle is  $153^{\circ}\pm 1^{\circ}$ . (c) SEM image of the leaf surface comprising almost-hemispherically-topped papillae with sizes  $5^{-10}$ mm with surface density of  $4^{\circ}\pm 105^{\circ}$  cm<sup>2</sup> (scale bar 10mm). (d) High magnification SEM image of a single papillous depicting branch like protrusions with sizes of about 150 nm (scale bar 1mm).

surfaces obtained by varying the irradiation parameters. Its morphology looks very similar to that of the Lotus leaf (**Figure 2(c) and (d)**) consisting of micro-scale conical features decorated with nano-scale protrusions. The protrusions in this case have conical or pyramidal asperities with average sizes of  $\sim 10$ mm and aspect ratio of  $\sim 4$ . Nanostructures of sizes up to a few hundred nanometers are clearly seen on the slopes of the protrusions (**Figure 2(d)**). Thus, the femtosecond laser irradiation under reactive SF<sub>6</sub> atmosphere was indeed able to produce a surface that mimics the structural features of the Lotus leaves as well as their water contact angle properties.

### 5.3 Bouncing experiments and analysis

In this section we study the dynamic behaviour of water drops impinging patterned Si surfaces in comparison to that of the lotus leaf and the untreated Si surface. We show that laser processing followed by chloroalkylsilane monolayer coating leads to the production of one of the most water repellent surfaces ever reported. We quantify the repellence of this surface and we directly compare it, to that of the natural lotus leaf, to find a remarkable similarity in the overall performance.

**Figure 5.4** presents the time evolution of the shape of water droplets impacting on the artificial structured silanized surface, such as that of **Figure 5.2**, in comparison to a Lotus leaf surface and to a silane coated flat Si surface. In particular, **Figure 5.4(a) and (b)** show a selected time sequence of snapshots of 10mL water droplets free-falling on the structured surface and on a Lotus leaf, respectively.. Following the weber number and restitution coefficient discussed in chapter 3 were studied for both the Si structured surface and natures lotus leaf. These drops impact the surface with a velocity that corresponds to a dimensionless Weber number of  $We=3.5$ . The behavior of the falling droplet is quite similar on the two surfaces. In particular, it is observed that the drop shape changes significantly during impact as its kinetic energy transforms into stored energy due to surface deformation. In these cases, the deformation is strong, because the Weber number, signifying the ratio of the arriving kinetic energy to the intrinsic surface energy, is higher than unity. Despite this deformation, both surfaces are so water-repellent that the drop bounces back numerous times (not shown here). **Figure 5.4(c)** and **d** show similar series of video frames of drops impacting the artificial structured silicon and the Lotus leaf surface, respectively, for  $We \leq 0.7 < 1$ , where the drop is lightly deformed: the similarity in the two cases is evident. On the other hand, no rebound is observed when the drop impacts on the flat (unstructured) region of a silanized silicon surface even for  $We \leq 3.5$  (**Figure. 5.4(e)**). In this case the surface is not water repellent and the drop has insufficient momentum to leave the sample; as a result it remains stuck to the surface.

The elasticity of the collisions observed on both the artificial laser structured surface and that of the natural Lotus leaf is remarkable, indicating a high degree of repellency. A direct measure of this elasticity is the restitution coefficient,  $e = V'/V$ , defined as the ratio of the center of mass velocity just after impact,  $V'$ , to that just before impact,  $V$ .

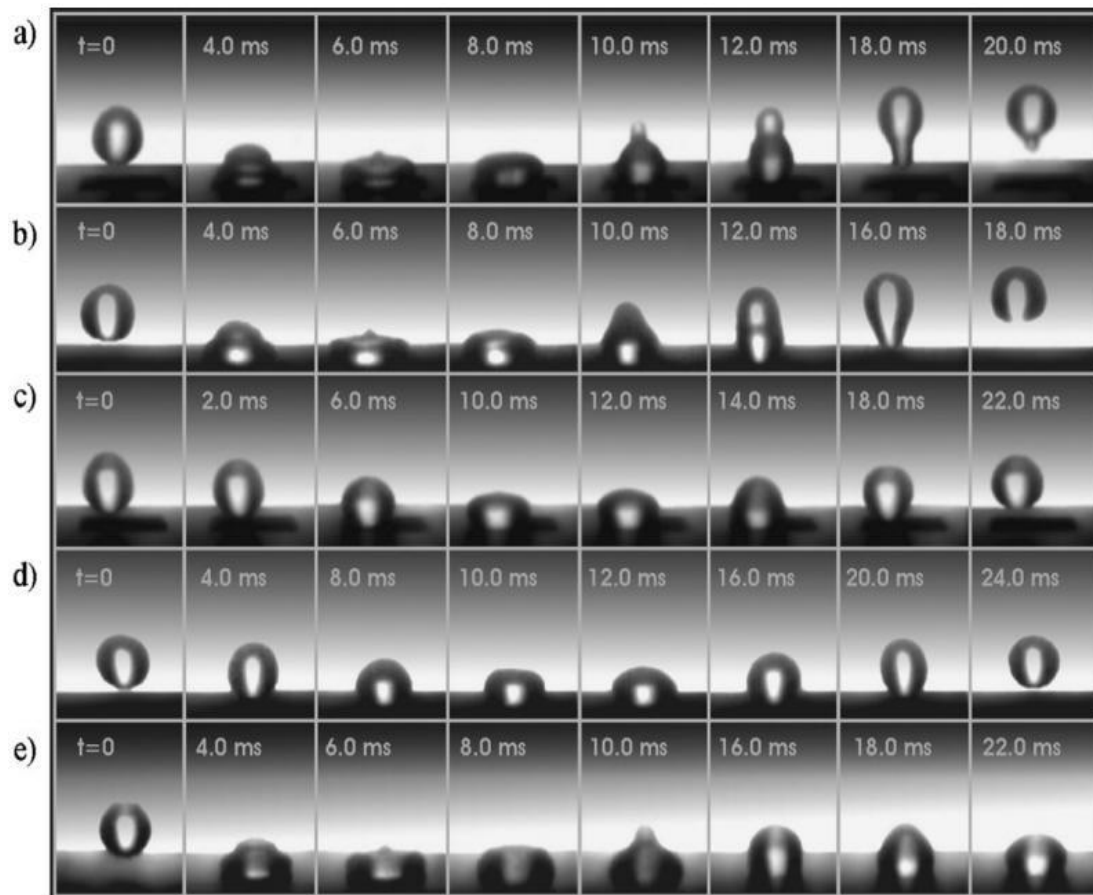


**Figure 5.4 :** Selected snapshots of a millimetric water drop impact on a lotus leaf, a flat and a laser structured Si surface. (a) on a laser structured Si surface with a Weber number,  $We$ , of 3.5, (b) on a lotus leaf surface with  $We= 3.5$ , (c) on a laser structured Si surface with  $We= 0.7$  (d) on a lotus leaf surface with  $We= 0.7$  and (e) on an unstructured Si surface with  $We= 3.5$ .

This coefficient was deduced from the recorded video images and is shown in **Figure 5.5** as a function of the impact velocity  $V$  for a series of experiments, performed with drops of different volumes. The highest elasticity is observed at intermediate velocities, from  $\sim 0.15\text{m/s}$  to  $\sim 0.25\text{m/s}$ , where the restitution coefficient is found to exceed 0.90. Its value matches that of the Lotus leaf and, to our knowledge, is among the highest ever reported.[9]. Elasticity arises from the efficient interchange between kinetic and surface energy during drop deformation. [8,40]. According to Richard and Quere,[9] even in the ideal case of zero energy loss during collision, there is a limit in elasticity,  $e < 1$ , due to the transfer of a part of kinetic energy into drop vibrations.[8] Indeed, in all cases it is observed that the droplet vibrated after leaving the surface. Thus, part of its initial kinetic energy is transferred into vibrational energy after the impact, and, subsequently, damping of the bouncing motion occurs due to viscous dissipation.

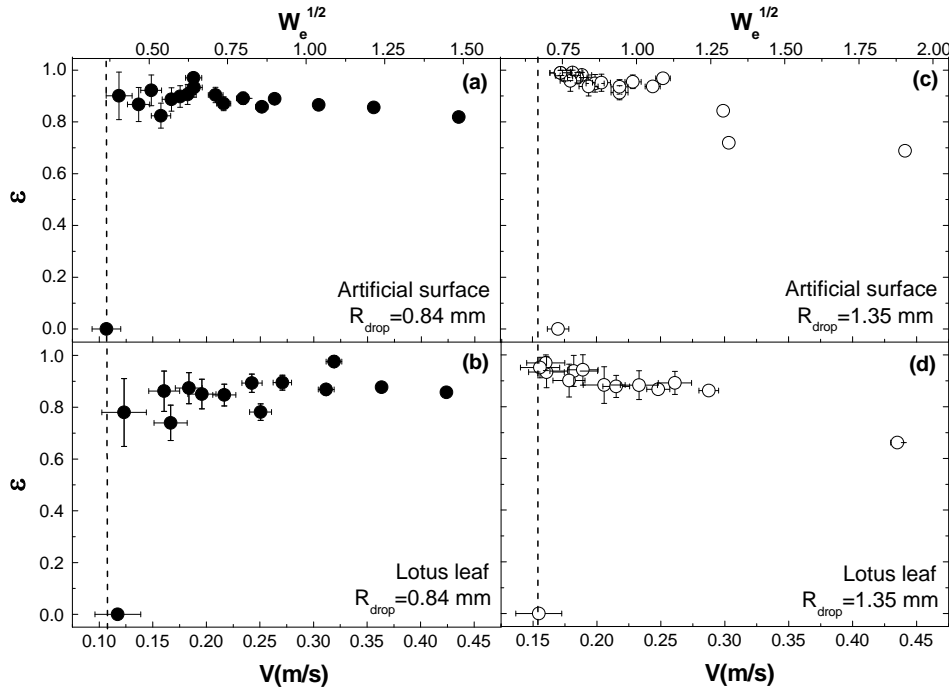


**Figure 5.5:** Restitution coefficient  $e = V'/V$ , where  $V'$  is the center of mass velocity right after impact and  $V$  that right before impact, as a function of the impact velocity  $V$  for an artificial silane-coated structured silicon surface (a,c) and a Lotus leaf surface (b,d) for two different sizes of falling water droplets with radii  $R$  of 0.84mm (a,b) and 1.35mm (c,d).

Although full rebounds occur at moderate impact velocities, the situation is different at small and large impact velocities  $V$ . For small velocities,  $e$  decreases abruptly with decreasing  $V$  and reaches zero at some velocity that depends on the droplet volume. This is the threshold that quantifies the water repellency of the surface; [40] the smaller this velocity, the more water repellent the surface is. The threshold velocity for the artificial surface is comparable to that of the Lotus leaf (**Figure 5.5**). The bouncing to non-bouncing transition arises from the presence of surface defects that become the main source of kinetic energy dissipation. The contact line pins on such defects resulting in a difference between the advancing and receding contact angles,  $\theta_a$  and  $\theta_r$ , i.e., in hysteresis. The bigger the droplet the longer this line is, resulting in higher hysteresis and, therefore, in an increase of the anticipated threshold velocity. This is exactly what is observed in **Figure 5.5** for both surfaces. The pinning force per unit length is [13,32,41]  $F = \gamma_{LV}(\cos \theta_r - \cos \theta_a) = \gamma_{LV} \Delta(\cos \theta)$ , with  $\gamma_{LV}$  the liquid surface tension; the energy dissipated will, thus, scale as  $\gamma_{LV} R^2 \Delta(\cos \theta)$ . The drop will bounce provided that its kinetic energy, which scales as  $rR^3 V^2$ , can overcome this dissipation. An estimate of the threshold velocity for water repellency can be obtained by equating the two energies. The relative contact angles were measured as  $\theta_a = 157^\circ$  and  $\theta_r$

$\theta = 152^\circ$  for the artificial structured silanized surface. For a drop with radius  $R \sim 0.84\text{mm}$ , the estimated threshold velocity is calculated as  $\sim 0.06\text{ m/s}$ , a value close to the one observed experimentally.

Finally, in the high velocity regime  $\theta$  slowly decreases with  $V$  because of the large drop deformation followed by increased internal vibration after impact. Studies on other structured surfaces have shown that there exists an upper velocity above which significant impalement of the drop occurs resulting in part of it getting captured to completely wet the surface.[41,42] The value of the highest velocity at which the surface remains dry has also been used as a measure of the surface resistance against wetting. In this context, the behavior of water droplets with impact velocities up to  $5\text{m/s}$ , a typical value for the terminal velocity of millimetric raindrops,[41] was examined. In this high velocity regime, the drop brakes apart into numerous smaller droplets (see Supporting Information, Movie 3S and Movie 4S). This behavior was never observed in the flat region of the silanized silicon sample, indicating that structuring favors the creation of tiny droplets in an effort to resist penetration by the falling drop. It is noted that the surface was thoroughly examined after each experiment with a high resolution CCD optical system for signs of water impalement. It was found that both the artificial structured surface and the Lotus leaf were impervious to water penetration over the entire range of attainable impact velocities ( $\sim 0.1\text{--}5\text{ m/s}$ ). Moreover, it should be emphasized that the low-adhesion and high repellency of the artificial surfaces are maintained even after rinsing and complete immersion in water for long periods of time. Long-term endurance against wetting is a feature that is always desirable in relevant applications.

## 5.5 Conclusions

In summary, a silicon-based water-repellent surface has been constructed, partially mimicking nature. The surface possesses a hierarchical morphology with two length-scale roughnesses combined with a proper hydrophobic chemistry. The water repelling characteristics of the surfaces were quantified by investigating the bouncing of free-falling water droplets impacting onto them as a function of impact velocity. This repellency of the artificial surface can be very favorably compared to that of the Lotus leaf in terms of the threshold velocity sufficient to avoid sticking of the droplets, the collision energy loss and the remnant wetting of the surfaces at high velocities. The great similarities observed in the water repellency between the artificial and Lotus leaf surfaces are indicative of the critical role of the two-scale hierarchical morphology, which combines microscale and nanoscale features. These results provide insight into the design of stable water repellent surfaces in Other materials, thus creating opportunities for various exciting applications.

# Chapter 6

## *Self Cleaning*

### 6.1 Introduction

The lotus plant's (**Chapter 5**) magnificent ability to repel dirt has inspired a range of self-cleaning and antibacterial technologies that may also help control microfluidic "lab-on-a-chip" devices. Microscopic bumps on a lotus leaf transform its waxy surface into an extremely water repellent, or superhydrophobic, material. Raindrops can roll easily across such a surface, removing any dust particles. Wilhelm Barthlott of the University of Bonn in Germany, is the discoverer and developer of the "lotus effect" . Barthlott realized that the effect is caused by the combination of two features of the leaf surface: its waxiness and the microscopic bumps (a few microns in size) that cover it. He knew from basic physics that the waxiness alone should make the leaves hydrophobic, or water repellent. On such a material, drops of water sit up high to minimize their area of contact with the material. Water on a more hydrophilic, substance spreads across it to maximize the contact area. For a hydrophilic surface, the contact angle (where the droplet's surface meets the material) is less than 90 degrees; a hydrophobic surface has a contact angle greater than 90 degrees. In addition, he understood that the innumerable bumps take things a step further and cause the lotus surface to be superhydrophobic—the contact angle exceeds 150 degrees, and water on it forms nearly spherical droplets with very little surface contact that roll across it as easily as ball bearings would. The water sits on top of the bumps like a person lying on a bed of nails. Air trapped between the water and the leaf surface in the spaces around the bumps increases the contact angle, an effect that is described by the Cassie-Baxter equation. (**Chapter 3**). In this chapter we will investigate the self-cleaning properties of the Si structure surfaces, by covering the tilted surface with carbon dust particles and letting a water drop roll over it. Secondly bouncing experiments were done as described in chapter 5, but with the Si surface covered again with carbon particles.

## 6.2 Experimental : Preparation of samples for self cleaning

Single crystal n-type Si (100) wafers with a resistivity of 2-8 Ohm-cm were placed inside a vacuum chamber that was first evacuated down to a base pressure of  $10^{-2}$ .  $\text{SF}_6$  gas was then introduced and maintained at a pressure of 500 Torr by means of a precision micro valve. The irradiating source was a regenerative amplified Ti:Sapphire laser (=800 nm) delivering 180 fs pulses at a repetition rate of 1 kHz and laser pulse fluence could be varied in the range of 0.37 to 2.50 J/cm<sup>2</sup>. Following the irradiation process, the patterned surfaces were covered by low surface energy organosilane layers, which are known to assemble high quality conformal coatings to flat Si surfaces. Spectroscopic ellipsometry measurements on the flat region of the samples show that the average thickness of the silane coating is about 2.5 nm. Detail of the structuring and silanization process can be found in **chapter 4**. **Figure 5.1 (a) and (b)** show a SEM micrograph of the silicon structure and a picture of the Lotus leaf surface where the similarity of the two structures is clearly observed. Both structures comprise micrometer-sized papillae decorated with nanometre-sized branch-like protrusions. Self cleaning properties were investigated by monitoring the behavior of a water droplet rolling and bouncing of a surface contaminated with carbon particles.

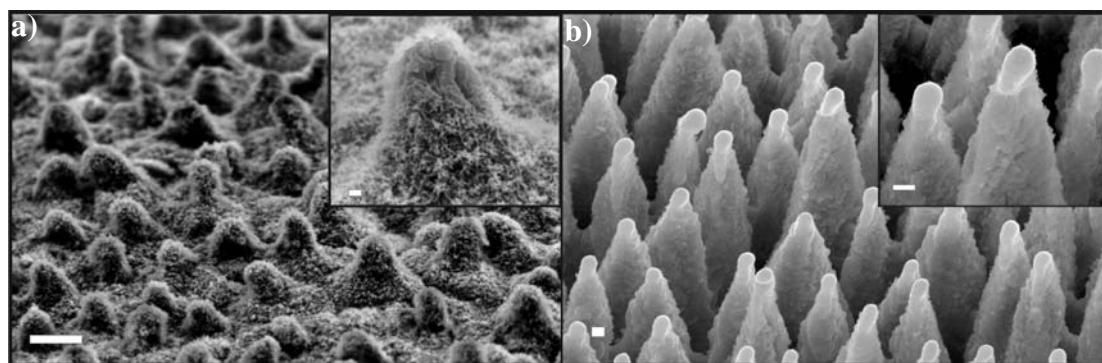


**Figure 6.1** : Side scanning electron microscope view of a) a lotus leaf (scale bar 10 $\mu\text{m}$ , 1 $\mu\text{m}$ ) and b) a Si structured surfaces (scale bar 5 $\mu\text{m}$ , 1 $\mu\text{m}$ ). The surface was irradiated by fs laser.

### 6.3 Self cleaning on a tilted surface

To confirm if the silicon structured surface has the same ability, the following experiment was performed. A slightly tilted structured surface was covered with carbon particles (**Figure 6.2a**) and a water drop was placed in order to roll over it. As it can be clearly seen from **Figure 6.2b** the water drop leaves a clean path behind it with nearly no particles as it rolled down the structured surface. It can be also seen (**Figure 6.2c**) that the drop at the end of its path, is surrounded by the carbon particles which were collected by it. By this we could simply demonstrate the self cleaning ability of the silicon structured surfaces.



**Figure 6.2:** (a) Silicon structured surface covered with carbon particles, (b) clean path left behind after the droplets rolling and (c) carbon particles collected by the drop.

### 6.4 Water drop bounce on dust covered surfaces

#### 6.4.1 Sample preparation

Similar bouncing experiments, as in chapter 5 were carried out, but with the Si surfaces covered with carbon dust particles. For this section four Si structured surfaces with different roughness were fabricated using different laser fluences (  $0.34 \text{ J/cm}^2$ ,  $0.56 \text{ J/cm}^2$ ,  $0.9 \text{ J/cm}^2$  and  $1.69 \text{ J/cm}^2$ ). All structures were covered with a hydrophobic monolayer, that is DMDCS, which details are described in **chapter 3**, followed by static contact angle measurements for each of the four surfaces. **Figure 6.3** shows the four different Si surfaces with the different morphology and below the

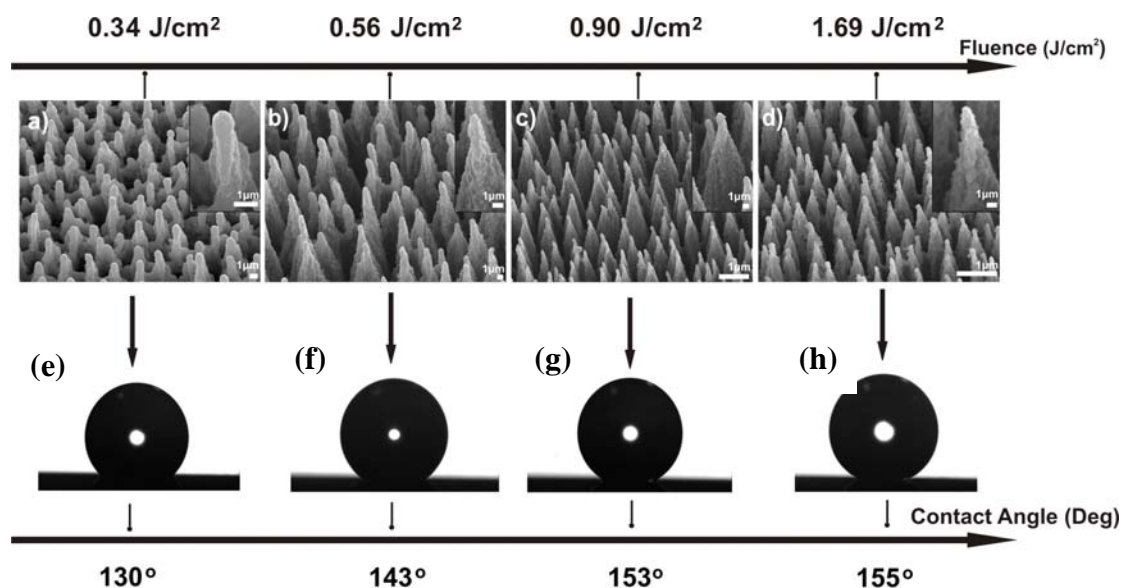


**Figure 6.3 :** a) – d) Side scanning electron microscope view of Si surfaces structured by fs-irradiation at different laser fluences. The insets are higher magnifications of the obtained structures. (e)-(h) Photographs of water droplets on the corresponding structured Si surfaces.

corresponding contact angle measured after the DMDCS coverage. The initial CA for the flat silicon is  $\sim 103^\circ$  (not shown here), and the starting CA for the surface fabricated at  $0.34 \text{ J/cm}^2$  is  $134^\circ$ . Finally the two surfaces build at  $0.9 \text{ J/cm}^2$  and  $1.69 \text{ J/cm}^2$  reach a CA above  $150^\circ$  making them superhydrophobic.

## 6.4.2 Bouncing experiments on dust covered surfaces

In this section we simulated the impact of a water drop falling on a dust covered Si surface. In this case similar bouncing experiments as discussed in chapter 5 were carried out. We first measured the restitution coefficient of these surfaces without covering them with dust. **Figure 6.4** shows a graph of the restitution coefficient measurements for a 10 ml water drop, for the four surfaces. As one clearly observes for velocities ranging from  $0.55 \text{ m/s}$  –  $0.85 \text{ m/s}$ , a similar behavior occurs for the most hydrophobic and hydrophilic surfaces. For these velocities the restitution coefficient takes values around 0.46. For even higher velocities, (meaning higher heights) the water drop breaks apart into smaller ones, making it impossible to take measurements, so velocities of around  $0.9 \text{ m/s}$  should be a plateau for the water drops.

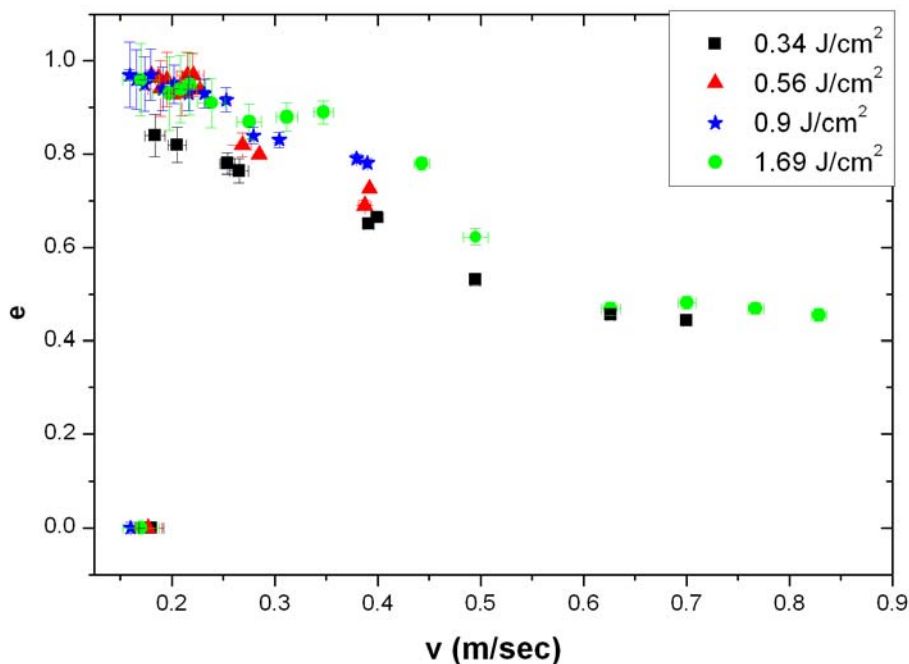


**Figure 6.4** : Restitution coefficient measurements for a 10 ml water drop, for the four surfaces fabricates at  $0.34 \text{ J/cm}^2$ ,  $0.56 \text{ J/cm}^2$ ,  $0.9 \text{ J/cm}^2$  and  $1.96 \text{ J/cm}^2$ .

The similar behavior of the RC observed for velocities higher than  $0.5 \text{ m/sec}$  is due to the high deformation of the water drop when it reaches the Si surface. As can be seen from **Figure 6.5** a greater amount of energy is lost due to the deformation of the water drop making the water drop incapable of rebounding to higher heights after the first one.

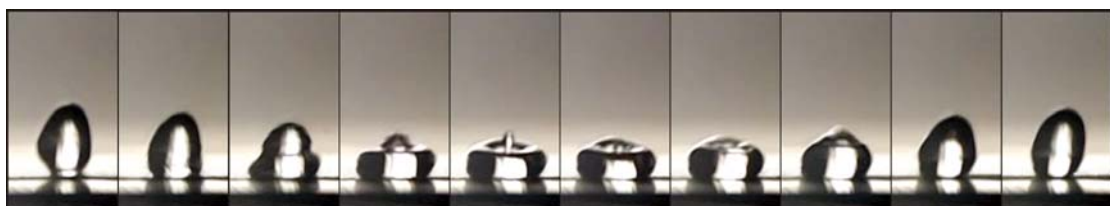


**Figure 6.5** : Selected snapshots of a 10ml water drop impact on a laser structured Si surface.

For velocities under  $0.5 \text{ m/s}$  we have a clear dissociation for the restitution coefficient for the four Si surfaces. For Si surfaces structured at  $0.34 \text{ J/cm}^2$  the RC reaches values up to

0.85, contrarily to the other three surfaces were the values can exceed 0.9, reaching up to 0.97 in some cases meaning that these surfaces are much more water repellent. The number of bounces observed for the structures at  $0.34 \text{ J/cm}^2$  was maximum four, much less that the other three were we could observe up to 9 bounces on the structured surface. For velocities around  $0.158 \text{ m/sec}$ , we have a threshold in which the RC is zero meaning that for this height the water drop is not bouncing by stases on the surface due to pinning forces.

**Figure 6.6** presents the RC measurements of the same set of surfaces, covered this time with carbon dust particles. The main difference observed here is in the very first bounce. All structures independently of the surface roughness have the same behavior, meaning that the RC is the same and has a value of around 0.62. This behavior occurs due to the carbon dust particles. On the first bounce the water drop bounces on a surface covered with dust, which decreases immediately its ability to reach higher heights the second time. This happens because there is a much greater pinning force acting on the water drop during the first impact due to the dust, which does not let the drop take higher RC values.

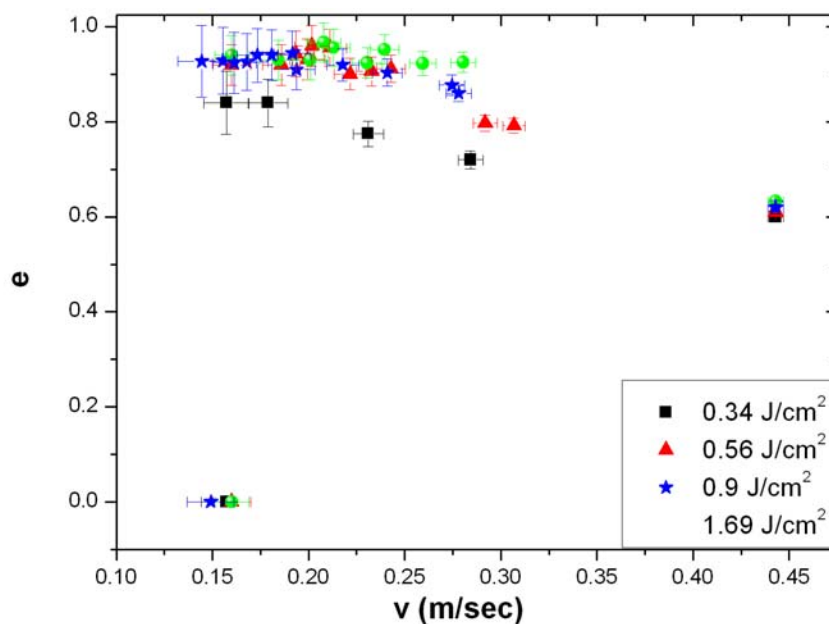


**Figure 6.6** : Restitution coefficient measurements for a 10 ml water drop bouncing on dust covered surfaces. The four surfaces are fabricates at  $0.34 \text{ J/cm}^2$ ,  $0.56 \text{ J/cm}^2$ ,  $0.9 \text{ J/cm}^2$  and  $1.96 \text{ J/cm}^2$ .

During the impact of the first bounce the water drop collects the carbon dust particles found under its volume and so the next bounces occur on a clean surface because the dust particles are surrounding the water drop this time, like in the self cleaning section (**Figure 6.2c**). As it can be seen the dust particles surrounding the water drop do not effect the RC afterwards, and take values very close to the ones with no dust particles.

## 6.5 Conclusions

The self cleaning ability observed on for the lotus leaf was also demonstrated of the silicon structured surfaces. Following the dynamic behavior of a free falling water drop was observed for different velocities. For high velocities a similar behavior in the RC was observed for all surface, giving identical values. For smaller velocities we have a clear dissociation for the restitution coefficient for the four Si surfaces distinguishing clearly the different hydrophilicity of the surfaces. Next the same bouncing experiment were carried out but covering the surfaces with dust particles. As it could be clearly seen during the impact of the first bounce the water drop collects the carbon dust particles found giving the same RC value for all four surfaces, and afterwards the values are distinguished the same.

# Chapter 7

## ***Reversible wettability of ZnO nanostructured thin films and hierarchical ZnO structures***

### 7.1 Introduction

Wettability has proved to be a defining property of solid surfaces and consequently has raised a lot of interest in the last decade. Wetting properties can be tailored by manipulating the chemistry and the geometric factors of the surface. The control of surface wettability is of great importance since for many applications it would be beneficial to be able to switch between hydrophobicity and hydrophilicity, via an external stimulus. This will lead to functional surfaces with applications from self-cleaning surfaces to drug delivery and lab-on-chip devices<sup>i,ii,iii</sup>. Along this line, it is known that many metal oxides can be photo-switched between the two wetting states when they are alternatively exposed to ultraviolet (UV) light and stored in the dark<sup>iv,v,vi</sup>. Among these metal oxides ZnO has drawn a lot of attention due to its outstanding optical and electrical properties. The photoinduced wettability of ZnO has been studied for different nanostructures<sup>vii,viii,ix,x</sup>. A variety of fabrication methods for ZnO nanomaterials has been reported in the literature, such as thermal evaporation<sup>xi</sup>, chemical vapour deposition<sup>xii</sup> etc. One of the simplest methods for growing high quality ZnO films<sup>xiii</sup>, as well as nanostructures<sup>xiv</sup>, with reproducible and controlled results has proved to be pulsed laser deposition (PLD).

### 7.2 ZnO nanostructured thin films

In the first section we describe the growth of ZnO nanostructures by pulsed laser deposition (PLD). In order to study the wetting properties, different surface morphologies have been obtained. Right after deposition, the samples were hydrophilic, however their contact angle always found to increase up to a constant value upon dark storage for a few days. After reaching its hydrophobic state, the samples could be turned to be hydrophilic by exposing them to UV light. This transition was found to be reversed upon dark storage or thermal heating. The time evolution of the observed reversible phenomena, between

hydrophobicity and hydrophilicity, is discussed in terms of the film properties induced by preparation conditions.

### 7.3 Experimental Details of ZnO nanostructured thin films

ZnO nanostructured thin films have been grown by a conventional pulsed laser deposition (PLD) method in flowing oxygen environment. A KrF excimer laser (Lambda Physik,  $\lambda=248$  nm,  $\tau=34$  ns pulse duration, 600 mJ/pulse maximum) was used for the ablation, delivering pulses at a repetition rate of 10 Hz. The beam was incident on a rotating target at an angle of  $45^\circ$  with respect to the target normal and was focused by a spherical lens to yield an energy fluence of  $1.5$  J/cm<sup>2</sup> per pulse. The base pressure prior to deposition was better than  $10^{-6}$  mbar. During deposition the partial oxygen pressure was in the range  $5 \times 10^{-4}$ – $5 \times 10^{-2}$  mbar. The ablated material was collected on crystalline Si substrates that were placed parallel to the target at a distance of 4 cm and heated up to  $650$  °C using a resistive heater. The sample was cooled to room temperature at the same oxidized environment as during deposition. The crystalline structure of the films was determined by X-ray-diffraction (XRD) measurements using a Rigaku D/MAX-2000H rotating anode (12 kW) Cu K $\alpha$  monochromated diffractometer. The films were measured at  $\theta/2\theta$  configuration. The morphology of the surfaces was characterised by a field emission scanning electron microscope (FESEM-JEOL 7000), and atomic force microscopy (AFM) in tapping mode. Static contact angle measurements were performed by an automated tensionmeter, using the sessile drop method. A  $2\mu\text{l}$  distilled, deionised Millipore water droplet was gently positioned on the surface using a microsyringe and images are captured to measure the angle of the liquid-solid interface.

Light induced hydrophilicity was studied by irradiating the samples at certain time intervals using a UV Xe lamp with an intensity of  $20$  mW cm<sup>-2</sup> at the position of the samples. After each time irradiation interval, a  $2\mu\text{l}$  water drop was placed on the irradiated area and the corresponding contact angle was measured. Following irradiation, the samples were either stored in the dark at ambient conditions or annealed for 1 h at  $200$  °C in ambient conditions. Subsequently, the respective evolution of the contact angles with time was determined.

## 7.4 Reversible wettability of ZnO nanostructured thin films

ZnO films have been deposited by PLD on Si substrates at high temperature, 650°C, at different oxygen partial pressures during deposition. **Figure 7.1** depicts the FE-SEM images of samples prepared at  $5 \times 10^{-4}$  (hereafter referred as Sample A),  $5 \times 10^{-3}$  (Sample B) and  $5 \times 10^{-2}$  (Sample C) mbar partial oxygen pressure. It is evident that while for low oxygen partial pressure the resulted film does not have nanostructured morphology, as the oxygen pressure increases, the surface attains well nanostructured morphology with well separated particles. Finally, oxygen pressure of  $5 \times 10^{-2}$  mbar results in the formation of a nanostructure comprising well shaped, almost hexagonal particles, covering uniformly the surface. The roughness of the surfaces has been measured by AFM measurements (images are not shown here for brevity). The increase in oxygen pressure results in the increase of surface roughness from 1nm for the sample prepared at lower oxygen pressure to 8nm for the sample grown at highest oxygen pressure, i.e. approximately one order of magnitude. **Figure 7.2** shows the XRD spectra of the samples. All diffraction spectra exhibit predominately the (002) reflection at  $\sim 34.4^\circ$ , indicating the wurtzite structure of the nanostructured films, with the c-axis oriented normal to the substrate, as well as their high degree of the stoichiometry.

The contact angle of the samples right after deposition was approximately  $45^\circ$  and increased to a stable value after dark storage for approximately 5 days. Thus an evolution of the surface energy of the films is taking place indicating that the as-deposited material is in a metastable state and is driven to a favored equilibrium state after interaction with the ambient. Thermal heating is observed to speed up this process towards hydrophobicity.

**Figure 7.3a** depicts the contact angle evolution with UV illumination time, of the three samples. The stabilized contact angle was  $73^\circ$  for the Sample A and increasing to approximately  $95^\circ$  from Samples B and C, which were grown at partial oxygen pressure of 1 and 2 higher orders of magnitude.

The wetting behaviour of a surface is described by the contact angle that a droplet forms when it rests on the surface. Since the roughness of all three samples is very small ( $< 10\text{nm}$ ), the contact angle ( $\theta$ ) is estimated by the simple Young's equation:

$$\cos \theta = (\gamma_{sg} - \gamma_{sl}) / \gamma_{lg}$$

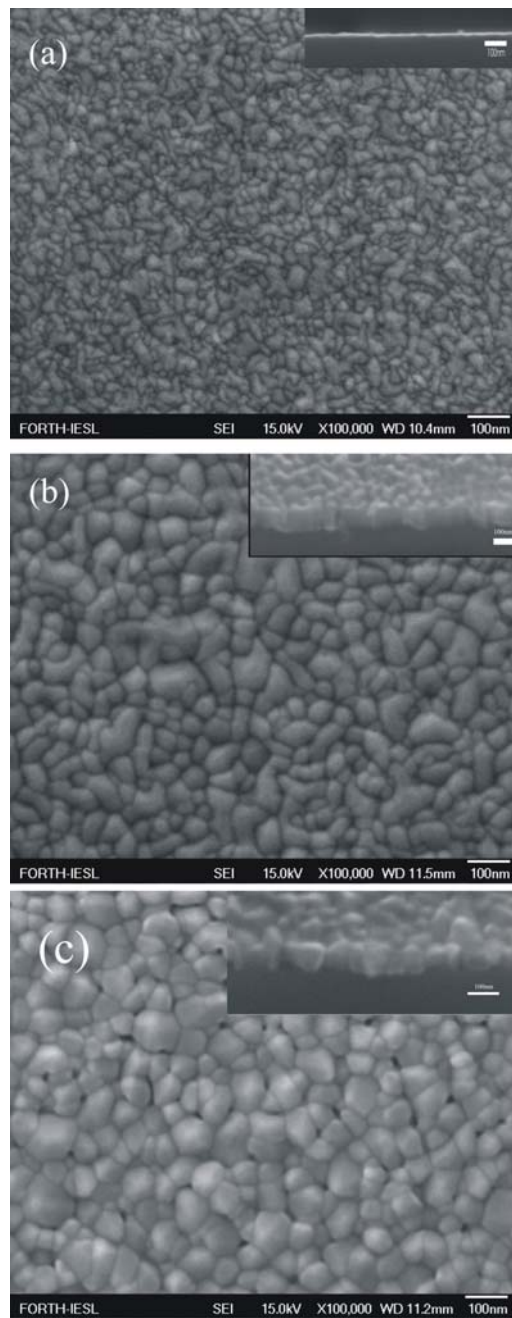


**Figure 7.1 :** Top view FE-SEM images of the samples prepared at (a)  $5 \times 10^{-4}$  mbar (b)  $5 \times 10^{-3}$  mbar and (c)  $5 \times 10^{-2}$  mbar of partial oxygen pressure. The insets depict the cross section images of the respective sample.

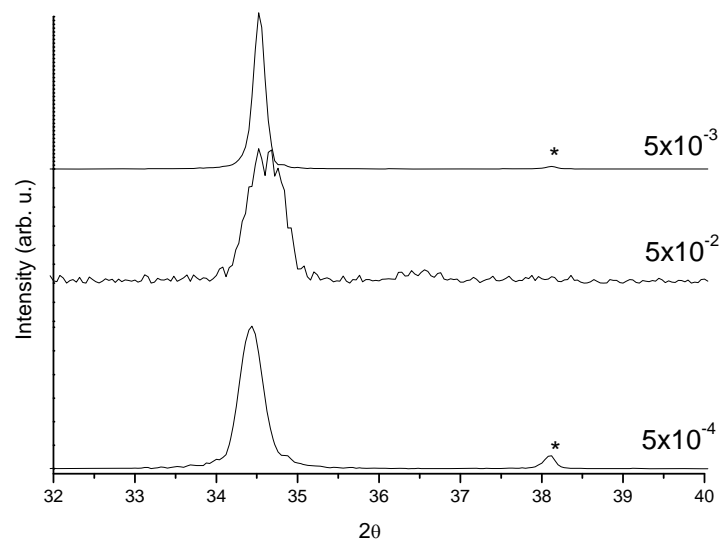


**Figure 7.2 :** The XRD spectra of ZnO nanostructured films shown on **Figure 7.1**. The asterisks denote peaks originating from the substrate.

where  $\gamma$  is the surface tension and the subscripts lg, sg and sl stand for the liquid-gas, solid-gas and solid-liquid interface, respectively. Thus the difference in the CA between the samples can be attributed to the change in the surface tensions  $-\gamma_{sl}, \gamma_{sg}$  between the surface and the water or air respectively.

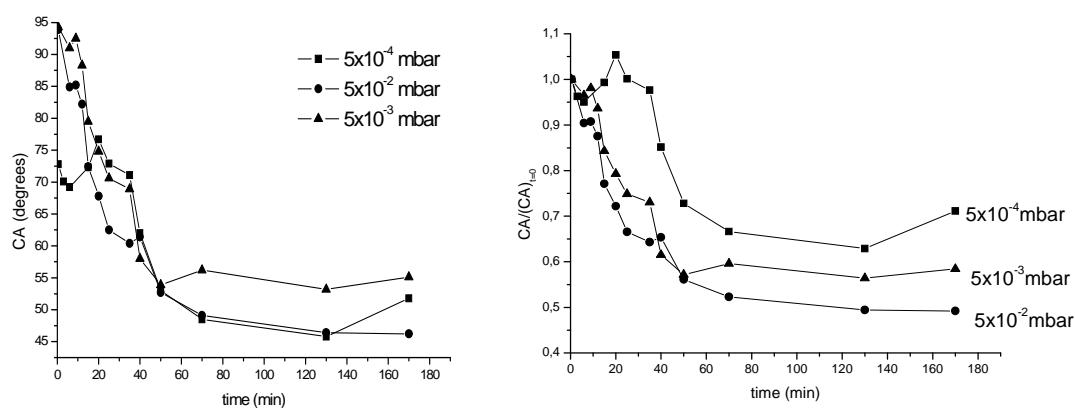


**Figure 7.3 :** Dependence of the water contact angle on the UV illumination time for the different nanostructures studied. The corresponding evolution of the ratio of the respective contact angles to their initial values is also plotted for comparison.

Under UV illumination sample A displays a rather weak response, reaching CA of  $\sim 45^\circ$  after 2h. Samples B and C also become hydrophilic after the same time of UV exposure, acquiring a contact angle lower than  $50^\circ$ . The relative changes are better understood in **Figure 7.3(b)**, where the normalised contact angle evolution, obtained by dividing each CA value to that at  $t=0$ , is shown. Evidently, the contact angle reduction rate, which is a measure of the efficiency of the light induced process, is higher for the nanostructured samples. It should be emphasised that the aforementioned changes in the wettability of the surfaces are reversible and storage in the dark as well as thermal heating at low temperature ( $200^\circ\text{C}$ ) have as a result the conversion of the surface to its original wetting state (**Figure 7.4**). Samples stored in the dark revert to their original wetting state after about 15 days of storage, whereas thermal heating speeds up the reversibility process to approximately 1 hour. Samples were subjected to numerous switching cycles and no deterioration was noted, neither regarding the reversibility behaviour, nor the illumination efficiency.

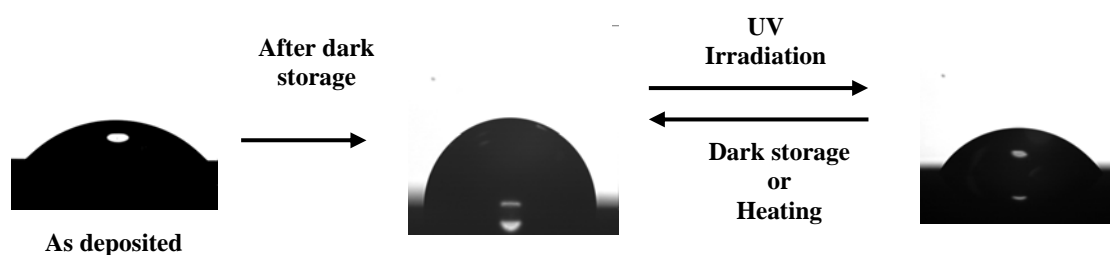


**Figure 7.4 :** Photographs of the shape of a water droplet on Sample B before (left) and after (right) UV illumination. The transition from hydrophobicity to superhydrophilicity is reversible upon dark storage or thermal heating

## 7.5 Photoinduced wettability conversion mechanism

The reversible switching between hydrophobicity and hydrophilicity is the synergistic effect between surface chemical composition and surface roughness. The former provides a photosensitive surface, which can be switched between hydrophilicity and hydrophobicity, while the latter further enhances these properties. In the present case, however, the roughness of all samples under investigation is too small to significantly enhance hydrophobicity. We can then safely conclude that the switching between the two wetting states is mainly due to surface chemistry, as we shall explain following.

The origin of photoinduced hydrophilicity has been explained in the frame of creation of oxygen vacancies<sup>iv</sup>. It is known that upon UV illumination electron-hole pairs<sup>xv</sup> are formed in the lattice. Some of the holes react with lattice oxygen to form surface oxygen vacancies, while the electrons can react with the metal ions ( $Zn^{2+}$ ) present in the lattice, forming  $Zn^+$  defective sites. In the mean time, water and oxygen may compete to dissociatively adsorb on these vacancies. The  $Zn^+$  defective sites are kinetically more favorable for hydroxyl adsorption than oxygen adsorption. The above enhance the surface hydrophilicity and the water contact angle is significantly reduced. It has also been demonstrated that the surface becomes energetically unstable after the hydroxyl adsorption. The oxygen adsorption is thermodynamically favored, thus oxygen is can create stronger bonds to the defect sites than the hydroxyl group.

Consequently, when a sample is placed in the dark after the UV illumination, oxygen atoms gradually replace the hydroxyl groups adsorbed on the defective sites. Subsequently, the surface evolves back to its original state (before any UV illumination), attaining the initial wetting state. Heat treatment accelerates the elimination of surface hydroxyl groups, and as a result, the hydrophilic surface reconverts quickly to the hydrophobic one.

In addition to the above, it is known that ZnO grown by PLD is oxygen deficient<sup>xvi</sup>, meaning that oxygen vacancies are present in the lattice of the as-prepared samples. The number of these oxygen vacancies reduces when the oxygen pressure during growth is increased. Thus, it is expected that Samples B and C, which were fabricated in high oxygen context will contain less oxygen vacancies. On the contrary, Sample A which was grown at low oxygen context will, presumably, contain more oxygen vacancies. Accordingly, Samples B and C are hydrophobic, whereas Sample A is hydrophilic. Furthermore, as previously reported<sup>xvii</sup>, the nanoscale roughness plays an important role to the efficiency of the light-induced process. This may be due to the fact that the surface to volume ratio is higher in this case and as a result the total interface between water and the grown ZnO structures is high. This leads to an effective increase of the photo-active defect sites, which are in contact with water molecules. This is in accordance with the present results, where the photoinduced wettability is more pronounced for the samples exhibiting higher nanoscale roughness.

## 7.6 Hierarchical ZnO structures

In this section a two step approach is developed in order to obtain a ZnO surface exhibiting roughness at two length scales. Micro-scale roughness, in the shape of spikes, is achieved on a Si wafer by structuring with fs laser pulses [xviii]. Nano-scale roughness is subsequently realized by coating the laser structured surface with ZnO nano-grains grown by Pulsed Laser Deposition (PLD) [xix]. Consequently, an enhancement of the nanoscale roughness is realized, and the final ZnO surface comprises hierarchical micro- and nano-structures. It was shown that UV light can induce superhydrophilicity in the hydrophobic structures, while the hydrophobic state can be restored by dark storage or low temperature heating in air. A sharp photoinduced transition between two distinct wetting states is taking place and its relation to roughness has been explained in the context of the Cassie Baxter (CB) and Wenzel theoretical models [xx,xxi]. The comparison of the rough surfaces to a nanostructured thin film, prepared by the same experimental conditions has also been realized.

## 7.7 Experimental Details of hierarchical ZnO structures

A two step method was developed for the fabrication of the ZnO nanostructures on the Si spikes. The first step involved microstructuring of the flat silicon (Si) surface using an ultrafast laser, under a reactive gas ( $\text{SF}_6$ ) atmosphere. Single crystal n-type Si(100) wafers with a resistivity of  $\rho=2-8$  Ohm cm were subjected to laser irradiation in a vacuum chamber evacuated down to a residual pressure of  $10^{-2}$  mbar. A constant  $\text{SF}_6$  pressure of 500 Torr was maintained during the process through a precision micro valve system. The irradiating laser source was constituted by a regenerative amplified Ti:Sapphire ( $\lambda=800$  nm) delivering 150 fs pulses at a repetition rate of 1 kHz. The sample was mounted on a high-precision X-Y translation stage normal to the incident laser beam. A mechanical shutter was synchronized to the translation stages, exposing each given spot on the Si surface to an average of 500 pulses. Two laser fluences were used for the Si structuring, namely 0.17 and 2.1 J/cm<sup>2</sup>. After laser irradiation, the microstructured surfaces were first cleaned in ultrasonic baths of trichloroethylene, acetone and methanol followed by a 10% HF aqueous treatment in order to remove the oxide grown on the surface. In the second step, the freshly prepared Si patterned

surfaces were coated by ZnO, using the conventional Pulsed Laser Deposition (PLD) technique, in flowing oxygen environment. A KrF excimer laser (Lambda Physik,  $\lambda = 248$  nm,  $\tau = 34$  ns pulse duration, 600 mJ/pulse maximum) was used for the ablation of a ZnO target, delivering 2500 pulses at a repetition rate of 10 Hz. The beam was incident on a rotating target at an angle of  $45^\circ$  with respect to the target normal and was focused by a spherical lens to yield an energy fluence of  $1.5 \text{ J/cm}^2$  per pulse. The base pressure prior to deposition was better than  $10^{-6}$  mbar, while the partial oxygen pressure during deposition was kept constant at  $5 \times 10^{-2}$  mbar. The Si substrate was placed parallel to the target at a distance of 4 cm and heated up to  $650^\circ\text{C}$  using a resistive heater. The samples were cooled to room temperature at the same oxidized environment as during deposition. In this work we have used three types of substrates, namely Sample A (the Si microstructure prepared at  $0.17 \text{ J/cm}^2$ ), Sample B (the Si microstructure prepared at  $2.1 \text{ J/cm}^2$ ) and a nanostructured thin film.

The morphology of the samples' surface, prior as well as after the deposition of ZnO, was characterised by field emission scanning electron microscopy (FESEM – JEOL 7000) equipped with an energy dispersive x-ray spectrometer (EDX). The latter was used for the study of the elemental composition of the samples. An image processing algorithm was implemented in order to obtain quantitative information concerning the topological characteristics of the formed structures i.e. spikes' density, height, cone tip radius and distribution, from top and side-view FESEM pictures of the structured areas.

The crystalline structure of the ZnO films was determined by X-ray-diffraction (XRD) measurements using a Rigaku D/MAX-2000H rotating anode (12 kW) Cu  $K_\alpha$  monochromated diffractometer. The films were measured at  $\theta/2\theta$  configuration. Static contact angle measurements were performed by an automated tensionmeter, using the sessile drop method. A  $2\mu\text{l}$  distilled, deionised Millipore water droplet was gently positioned on the surface using a microsyringe and images were captured to measure the angle formed at the liquid-solid interface. The light induced hydrophilicity was studied by irradiating the samples for certain time intervals using selective fs pulsed UV laser irradiation (248 nm), with an intensity of  $14 \text{ mW cm}^{-2}$ . A monochromatic pulsed laser source is a preferable alternative to conventional UV lamps in terms of photoconversion efficiency, since the process can be significantly accelerated, while avoiding a wider spectral distribution which often includes unwanted visible wavelengths, known to inhibit the photoinduced transition [xxii]. After each irradiation interval, a  $2\mu\text{l}$  water drop was placed on the irradiated area and the corresponding contact angle was measured. Following irradiation, the samples were either stored in the dark

at room temperature or annealed for 1 h at 200 °C in ambient conditions. Subsequently, the respective time dependent contact angle variations were determined.

## 7.8 Reversible wettability of hierarchical ZnO structures

The laser irradiation creates a surface morphology comprising a highly uniform and densely packed array of micrometer sized conical structures (spikes). At higher laser fluence, the spike aspect ratio increases, resulting in a significant enhancement of the overall roughness [20]. **Figure 7.5(a)** shows FESEM pictures of the microstructured silicon surfaces. As we have previously reported [xviii], fs laser structuring at different fluences allows one to control the wetting properties of Si surfaces. The water contact angle increases with laser fluence from 65° (flat Si) to ~129° for the surface prepared at 0.17 J/cm<sup>2</sup> and to ~150° for the surface prepared at 2.1 J/cm<sup>2</sup>. The surface morphology of a ZnO thin film deposited on a flat Si substrate is presented in **Figure 7.5(b)**. It consists of nanosized grains, average diameter of approximately 50 nm, with a regular, hexagonal shape. The corresponding cross-sectional view depicts the columnar structure of the grains, suggesting that the film growth has a preferred orientation, perpendicular to the substrate plane. X-ray diffraction analysis confirmed that the as-deposited ZnO film is highly oriented along the (0 0 2) direction. Other orientations corresponding to (1 0 0) and (1 0 1) are present with very low relative intensities. In the as-deposited state, the ZnO film is hydrophilic exhibiting a contact angle close to 80°. **Figure 7.5(c) and (d)** depicts FE-SEM images of the morphology of Samples A (**Figure 7.7(a)**) and B (**Figure 7.7(b)**), as acquired after the deposition of the nano-grained ZnO film. As clearly seen, a significant enhancement of the nanoscale roughness is attained. The micrometer scale spikes have been decorated by nano-sized protrusions, resulting in a hierarchically rough surface. The nanoscale features are more pronounced in Sample A, than in Sample B. The corresponding contact angles were measured to be ~120° for Sample A and ~140° for Sample B. The stoichiometry of the ZnO protrusions was confirmed by EDX measurements performed on different positions on the structured surfaces (**Figure 7.5(e)**).

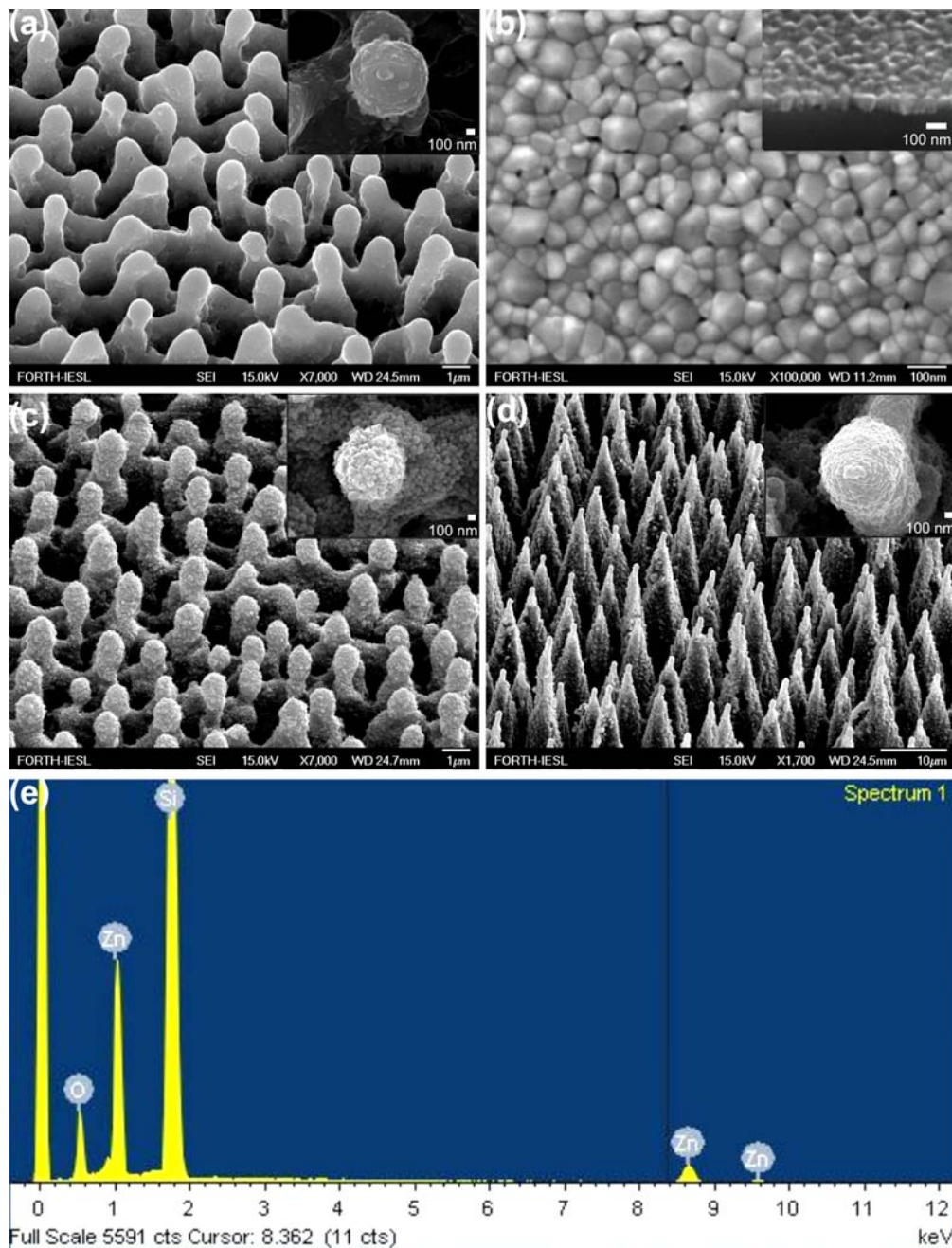


**Figure 7.5 :** (a) Side SEM view of Si surfaces structured by fs irradiation at laser fluence of  $0.17 \text{ J/cm}^2$ . The inset shows a higher magnification of the top of a single micro-cone; (b) Top SEM view of a nano-grained ZnO film prepared by PLD on a flat Si substrate. A cross-sectional image of the film is shown in the inset; (c) Side SEM view of a ZnO coated Si surface structured by fs irradiation at laser fluence of  $0.17 \text{ J/cm}^2$ . Higher magnification of the top of a single micro-cone (the scale bar is 100nm), shown in the inset, reveals the double scale roughness of the structures; (d) The same as in a) but at laser fluence of  $2.1 \text{ J/cm}^2$ ; (e) Typical EDX spectrum from a ZnO coated Si spike surface. Elemental analysis showed a 1.0 : 1.05 molar ratio of Zn and  $\text{O}_2$  respectively.

The elemental analysis of the EDX spectrum was found to be similar to that obtained in the flat part of the sample outside the spikes area. In both cases, the ZnO coating was deposited at identical conditions to that used for the nanostructured thin film shown in **Figure 7.5(b)**.

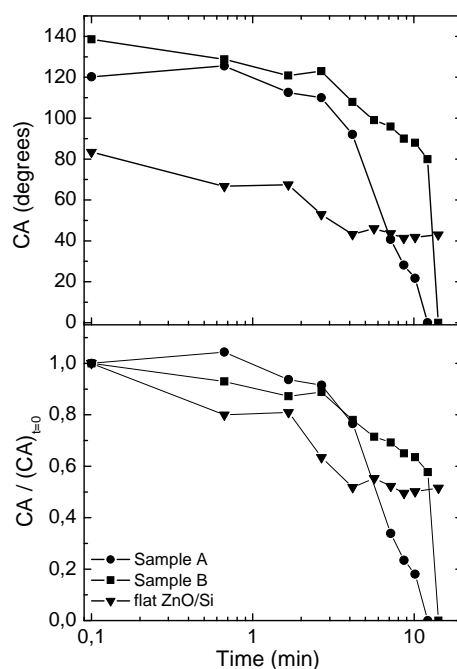


**Figure 7.6** : Dependence of the water contact angle on the UV illumination time for the flat and the structured ZnO samples studied. The corresponding evolution of the ratio of the respective contact angles to their initial values is also plotted for comparison.

**Figure 7.6** depicts the contact angle evolution with UV irradiation time for the different ZnO structures employed. Both structured samples exhibit a significant photo-induced transition to super-hydrophilicity, reaching a nearly zero contact angle in short time. More importantly, the contact angle reduction rate, being a measure of the efficiency of the light induced process, is higher than that observed in other ZnO structures [xxiii]. Counter-intuitively, this rate is lower for Sample B, which exhibits higher total roughness, as will be shown later. On the contrary, the nanostructured ZnO thin film shows a weak response to UV irradiation, as the wetting angle change in this case is much smaller for the same irradiation time.

It should be emphasized that the aforementioned wettability changes are reversible, since both dark storage and thermal heating reconverts the super-hydrophilic surfaces to their original states, as shown in **Figure 7.7(a)**. After the UV irradiation, the samples were placed in the dark. The hydrophobicity for Samples A and B was restored within 24 hours, whereas the flat sample requires 7 days storage in order to return to its initial wetting state (**Figure**

7.7(b)). Alternatively, thermal heating at 200 °C for 1h can return all surfaces to their original hydrophobic state, speeding up the reversibility process. All samples were subjected to numerous switching cycles (Figure 7.7(c)), without observing any deterioration of either the irradiation efficiency or the reversibility behaviour.

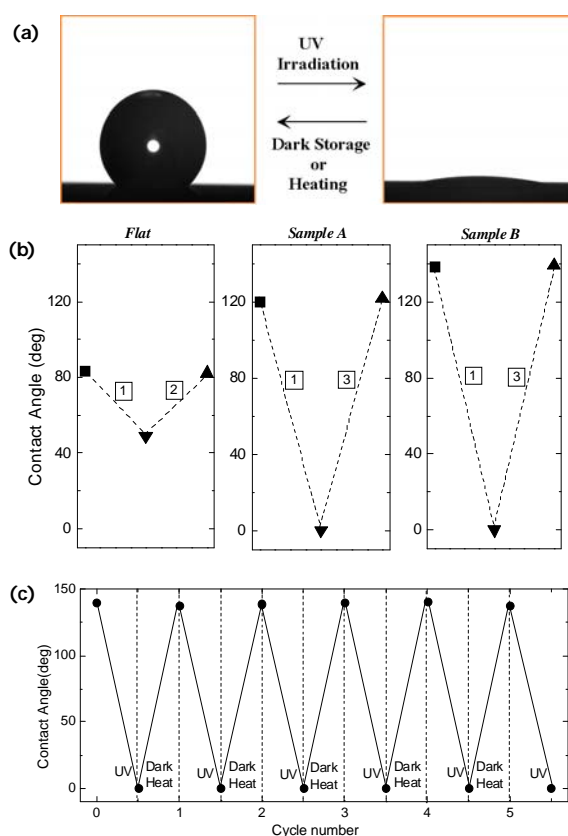


**Figure 7.7 :** (a) Photographs of the shape of a water droplet on Sample B before (left) and after (right) UV illumination. (b) Restoration of the UV light-induced wettability conversion upon sample storage in the dark. The processes 1, 2 and 3 denote UV illumination for 20min and dark storage for 7 and 1 days respectively. In all cases, the surface can be switched several times between the two states, under the alternation of UV irradiation and dark storage. (c) Reversible switch from hydrophobicity to super-hydrophilicity for the Sample B, under the alternation of UV irradiation and thermal heating at 200 °C for 1 hour. Sample A exhibits similar response.

## 7.9 Contribution of roughness in the photoinduced transitions

In order to understand the response of the as-deposited structures, one has to consider the effect of the macroscopic surface roughness on the wettability, which has been theoretically approached by two different models. In the *Wenzel* model [xxi], the liquid is assumed to completely penetrate within the rough surface and the apparent contact angle,  $\theta_w$ , is given by:

$$\cos \theta_w = r_w \cos \theta \quad (\text{Eq. 7.1})$$

where  $r_w$  is the ratio of the actual over the projected surface area of the substrate, and  $\theta$  is the intrinsic contact angle on a flat surface of the same nature as the rough. Since  $r_w$  is always greater than unity, this model predicts that the contact angle of a liquid that wets a solid ( $\theta < 90^\circ$ ) decreases when its surface is roughened ( $\theta_w < \theta$ ) while, roughening a non-wetting flat surface ( $\theta > 90^\circ$ ) always increases its hydrophobicity ( $\theta_w > \theta$ ). In contrast, Cassie and Baxter [xx] assumed that the liquid does not completely permeate the roughened solid. As a result, air pockets are trapped inside the features underneath the liquid, which sits above a composite surface made of solid and air. In this case, the contact angle,  $\theta_{CB}$ , is an average between the value on air (i.e.  $180^\circ$ ) and the value on the flat solid (i.e.  $\theta$ ) and is given by:

$$\cos \theta_{CB} = -1 + f(1 + \cos \theta) \quad (\text{Eq. 7.2})$$

where  $f$  defines the fraction of the projected solid surface wetted by the liquid. As  $f$  is always lower than unity, this model always predicts enhancement of hydrophobicity, independent of the value of the initial contact angle  $\theta$ . The lower the value of  $f$ , the smaller the solid-liquid contact area and the higher the increase in the measured contact angle. The effect of double scale roughness on wettability has been recently addressed [xxiv,xxv,xxvi]. Assuming that the two types of roughness are homothetic [**Error! Bookmark not defined.**], meaning that they occupy the same fraction of surface,  $f$ , the Cassie-Baxter equation is modified as follows:

$$\cos \theta'_{CB} = -1 + f^2(1 + \cos \theta) \quad (\text{Eq. 7.3})$$

As  $f < 1$ , the comparison of Eq. (2) and (3) shows that the contact angle of the dual roughness surface is always higher than in the single roughness case. There are many theoretical and experimental reports on the transition between the two basic wetting states described above,

under the action of various external stimuli [xxvii,xxviii,xxix,xxx]. However, to our knowledge, there are no reports for the effect of different roughness scales on the characteristics of this transition.

The initial contact angle of the flat ZnO sample is always lower than  $90^\circ$  indicating that the as-deposited grains are hydrophilic. Following the results presented in **Figure 7.6**, it is obvious that the original contact angle values measured for the structured samples are consistent with the CB model, since this is the only one predicting a rise in the wetting angle upon increasing the roughness of an initially hydrophilic ( $\theta < 90^\circ$ ) surface.

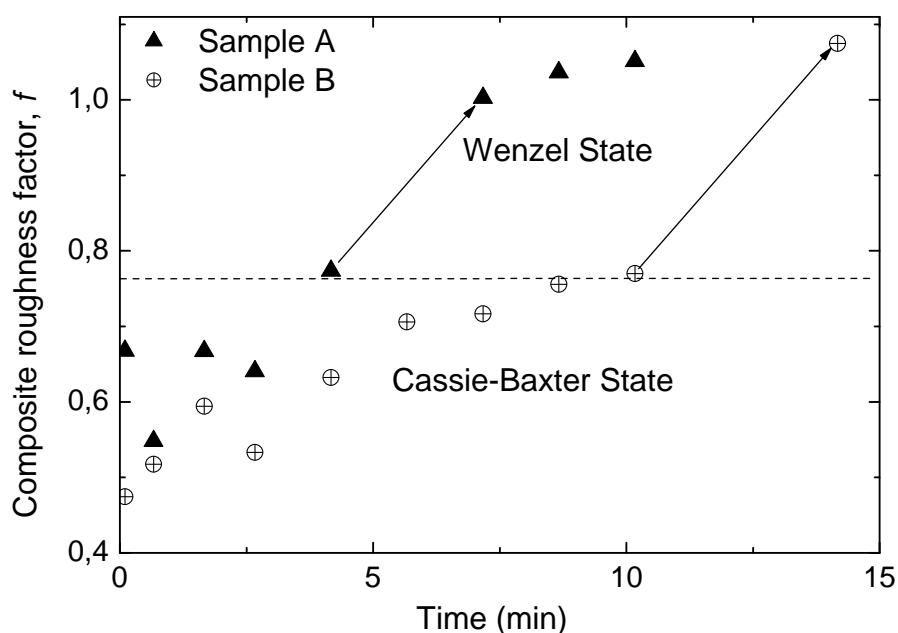


**Figure 7.8** : Dependence of composite roughness factor,  $f$ , on the UV-irradiation time for the samples A and B, respectively. The transition from the Cassie Baxter to the Wenzel state occurs at a critical  $f$  denoted by the dashed line.

Assuming that the intrinsic contact angle  $\theta$  is that measured on the flat film, i.e. equal to  $83.4^\circ$ , Eq. (3) is used for the estimation of the  $f$  parameter for the two samples in their as-deposited state. The result is  $f \sim 0.7$  for Sample A, and  $f \sim 0.5$  for Sample B. This means that Sample B exhibits higher total roughness and, being in a Cassie-Baxter state, is less wetted by the water drop.

As also shown in **Figure 7.6**, in both samples the evolution of contact angles is gradual at short illumination times, followed by an abrupt change taking place at wetting angles lower than  $\sim 90^\circ$ . This sharp transition towards super-hydrophilicity suggests that the

wetting state of the drop switches from the Cassie-Baxter to the Wenzel one, as the latter is the model predicting the possibility of super-hydrophilicity for very rough surfaces. The corresponding evolution of the composite roughness factor  $f$  up to the transition to the Wenzel state can be monitored using Eq. 3 and the contact angle values of **Figure 7.6**. This is plotted in **Figure 7.8** where each point of the factor  $f$  had been obtained by substitution in Eq. 3 of the respective contact angle values for any given exposure time. As can be seen from this plot, the transition takes place when  $f$  takes values higher than unity, rendering the Cassie-Baxter model invalid.

As can be shown in **Figures 7.6 and 7.8** the final step to superhydrophilicity is more abrupt in the case of Sample B where the microscale roughness is higher. This suggests that microscale roughness plays a major role for the transition from the Cassie-Baxter to Wenzel state as it contributes more to the total roughness. On the contrary, the transition to Wenzel state occurs in shorter times for Sample A where the nanoscale roughness is more pronounced. This indicates that nanoscale roughness plays a more important role to the efficiency of the light-induced process. This may be attributed to the fact that the surface to volume ratio is higher in this case and as a result the total interface between water and the grown ZnO structures is high. This leads to an effective increase of the photo-active defect sites, which are in contact with water molecules.

The mechanism of the photoinduced wettability is as discussed in the section 7.4

## 7.10 Conclusions

ZnO nanostructured, thin films were grown by PLD, using different oxygen pressures during growth. The initial wetting state of the samples was found to depend on the oxygen during growth. In addition, despite the fact that surface roughness was not found to play an important role in the wetting properties of the samples, it was shown that the oxygen context during growth is a parameter that essentially changes the surface chemistry, inducing reversible, photo-induced hydrophilicity.

A two-step method was developed to prepare ZnO structures showing hierarchical architectures combining microscale and nanoscale features. Such ZnO structures were found to exhibit a remarkable reversible transition to super-hydrophilicity after exposure to UV light. We conclude that this technique can be employed to control the structural and morphological properties of ZnO structures, resulting in reversible efficient wettability changes. Such capability may be useful for self-cleaning coatings and microfluidic applications, as well as for studying the wettability of biological surfaces and its relation to micro- and nanostructures.

- <sup>i</sup> O. D. Velev, B. G. Prevo, K. H. Bhatt, *Nature* **426**, 515 (2003).
- <sup>ii</sup> N. Verplanck, Y. Coffinier, V. Thomy, R. Boukherroub, *Nanoscale Res. Lett.* **2** 577 (2007).
- <sup>iii</sup> V. Zorba, E. Stratakis, M. Barberoglou, E. Spanakis, P. Tzanetakis, S. H. Anastasiadis, C. Fotakis, *Adv. Mater.* DOI: 10.1002/adma.200800651 (2008).
- <sup>iv</sup> R. Sun, A. Nakajima, A. Fujishima, T. Wanatabe, K. Hashimoto, *J. Phys. Chem. B* **105** 1984 (2001).
- <sup>v</sup> M. Miyauchi, A. Nakajima, T. Watanabe, and K. Hashimoto, *Chem. Mater.* **14**, 2812 (2002).
- <sup>vi</sup> X. Feng, J. Zhai, and L. Jiang, *Angew. Chem. Int. Ed.* **44**, 5115 (2005).
- <sup>vii</sup> X. Feng, L. Feng, M. Jin, J. Zhai, L. Jiang, and D. Zhu, *J. Am. Chem. Soc.* **126**, 62 (2004).
- <sup>viii</sup> C. Badre, T. Pauporte, M. Turmine, and D. Lincot, *Nanotechnology* **18**, 365705 (2007).
- <sup>ix</sup> C. S. Lao, Y. Li, C. P. Wong, and Z. L. Wang, *Nano Lett.* **7**, 1323 (2007).
- <sup>x</sup> G. Kenanakis, E. Stratakis, K. Vlachou, D. Vernardou, E. Koudoumas, N. Katsarakis, *Appl. Surf. Sci.* **254**, 5695 (2008).
- <sup>xi</sup> Z.W. Pan, Z.R. Dai, Z.L. Wang, *Science* **291**, 1947 (2001).
- <sup>xii</sup> M.H. Huang, S. Mao, H. Feick, H. Yan, Y. Wu, H. Kind, E. Weber, R. Russo, P. Yang, *Science* **292**, 1897 (2001).
- <sup>xiii</sup> E.L. Papadopoulou, M. Varda, K. Kouroupis-Agalou, M. Androulidaki, E. Chikoidze, P. Galtier, G. Huyberechts, E. Aperathitis, *Thin Solid Films* **516**, 8141 (2008).
- <sup>xiv</sup> Ye Sun, Gareth M. Fuge and Michael N.R. Ashfold, *Chem. Phys. Lett.* **396**, 21 (2004).
- <sup>xv</sup> E. Spanakis, E. Stratakis, P. Tzanetakis, H. Fritzsche, S. Guha and J. Yang, *Journal of Non-Crystalline Solids* 299-302 521 (2002).
- <sup>xvi</sup> B.J. Jin, S.H.s Bae, S.Y. Lee, S. Im, *Materials Science and Engineering B* **71**, 301 (2000).289\*/65
- <sup>xvii</sup> E.L. Papadopoulou, M. Barberoglou, V. Zorba, A. Manousaki, A. Pagozidis, E. Stratakis and C. Fotakis (submitted to *J. Phys. Chem. C*).
- <sup>xviii</sup> V. Zorba, L. Persano, D. Pisignano, A. Athanassiou, E. Stratakis, R. Cingolani, P. Tzanetakis and C. Fotakis, *Nanotechnology* **17**, 3234 (2006).
- <sup>xix</sup> E.L. Papadopoulou, M. Varda, K. Kouroupis-Agalou, M. Androulidaki, E. Chikoidze, P. Galtier, G. Huyberechts, E. Aperathitis, *Thin Solid Films* **516**, 8141 (2008).
- <sup>xx</sup> A.B.D. Cassie, S. Baxter, *Trans. Faraday Soc.* **40**, 546 (1944)
- <sup>xxi</sup> R. N. Wenzel, *Ind. Eng. Chem.* **28**, 988 (1936)
- <sup>xxii</sup> V. Rico, C. Lopez, A. Borrás, J. P. Espinos, A.R. Gonzalez-Elipé, *Solar Energy Materials & Solar Cells*, **90** (2006) 2944.
- <sup>xxiii</sup> R. Sun, A. Nakajima, A. Fujishima, T. Wanatabe, K. Hashimoto, *J. Phys. Chem. B*, **105** (2001) 1984.
- <sup>xxiv</sup> M. Nosonovskya, B. Bhushan, *Ultramicroscopy* **107**, 969 (2007).
- <sup>xxv</sup> N. A. Patankar, *Langmuir* **20**, 8209 (2004).
- <sup>xxvi</sup> S. Shibuichi, T. Onda, N. Satoh, and K. Tsujii, *J. Phys. Chem.* **100**, 19512 (1996).
- <sup>xxvii</sup> A. Lafuma, D. Quere, *Nature Mater.* **2**, 457 (2002).
- <sup>xxviii</sup> M. Sbragaglia, A. M. Peters, C. Pirat, B. M. Borkent, R. G. H. Lammertink, M. Wessling, D. Lohse, *Phys. Rev. Lett.* **99**, 15601 (2007).
- <sup>xxix</sup> E. Bormashenko, R. Pogreb, G. Whyman, M. Erlich, *Langmuir* **23**, 6501 (2007).
- <sup>xxx</sup> C. Dorrer and J. Ruhe, *Langmuir* **23**, 3820 (2007).

# Chapter 8

## *Nanostructures on bulk Al via its ablation in air and liquids*

### 7.1 Introduction

Metal NS have recently become the focus of research interest because of their unique properties, which differ from those observed for metals in bulk form. These properties depend on the size, shape and differences in the NS environments [1-3]. As a consequence, metallic NS are potential candidates for various applications in areas such as catalysis, and life sciences [4, 5]. Additionally, metal NS are known to exhibit distinctive optical characteristics, such as surface-enhanced Raman scattering (SERS) and second harmonic generation (SHG), relative to the bulk form of metals [6, 7]; several optoelectronic fields inspired by metal nanoparticles (NP) are also emerging, such as multiphoton absorption and fluorescence excitation for microscopy, microfabrication and optical data storage [8], and surface-plasmon enhanced light absorption for photovoltaic materials [9]. Finally, metal NS are of interest as a possible fuel in advanced energetic material applications, including propellants, munitions, and pyrotechnics and as additives for plastics, and powder metallurgy [10].

Laser ablation of solids in liquids is an efficient way for the generation of a large variety of metallic NS [11] and NP. Under sufficiently high laser fluence the surface of the target melts, and the melt is subsequently dispersed into the surrounding liquid under the recoil pressure of its vapour. On the other hand, at fluences close to the melting threshold of the material, short laser pulses with duration of less than a nanosecond (ns) melt only the micro-protrusions on the target surface giving rise to efficient formation of NS [12]. These NS are self-assembled since their period is several orders of magnitude smaller than the laser spot size ranging from 50 through 300 nm, depending on the target material. So far, NS have been realized on Ag, Au, and Ta in this way [13]. Formation of NS on both Ag and Au leads to visible coloration of both the exposed areas of the target or the liquid, and the colour is determined by the position of the plasmon resonance of the free electrons in the nano-relief. The principal advantage of laser ablation in comparison with chemical methods is a lesser need to add surfactant for capping of NS or NP so more pure nano-entities can be achieved.

Aluminum NS have attracted considerable interest as a candidate material in advanced energetic material [14] and optoelectronic applications [15, 16]. One of the major impediments to their use is that bare aluminum is highly reactive. It has also been found that

the reactivity of aluminum NS is greatly enhanced with decreasing size, resulting from the increased surface area-to-volume ratio [17]. This is the main reason that the experimental synthesis of Al NP is a complicated issue and stable nanosized aluminium has been rarely realised so far. The usual way to reduce the reactivity is to passivate the surface with a thin oxide layer. However, as particle size decreases, the oxide layer represents a significant fraction of the mass of the particle. In this context, ablation of Al in liquid environment with ns laser pulses leads to its unavoidable interaction with the liquid and the oxygen dissolved in it [18]. On the contrary, shorter laser pulses may help towards faster quenching of the nanostructured Al and thus preserve its metallic nature due to the shorter time of interaction with the liquid environment. In this communication we report on the successful nanostructuring of bulk Al targets in liquids- water or ethanol - and air under its irradiation using femtosecond laser pulses. It is observed that laser exposure results in the formation of self-organized nanostructures (nano-bumps) with an average period of 200 nm. Ablation of an Al target in liquid causes a dispersion of Al nanoparticles (NPs) into it. NS formed on the Al target as well as NP dispersions show a characteristic absorption in the near UV which has been attributed to plasmon oscillation of electrons. The edge of this peak extending to the visible, lead to a distinct yellow coloration of the processed Al surface and the liquid dispersions. Ultrafast laser structuring of bulk aluminum in fluids may be potentially a promising technique for efficient production of surface passivated nanosized aluminum.

## **8.2 Experimental procedure**

Prior to irradiation, Al targets with purity ranged from 95% to 75% were washed with ethanol and deionised water to remove organic compounds in a ultrasonic cleaner. A regenerative amplified Ti:sapphire fs laser with a repetition rate of 1 kHz, pulse duration of 180 fs and wavelength of 800 nm has been used for the generation of self-assembled NS on these targets. Irradiations were performed into air or while the sample was immersed into water and ethanol. The Al targets were mounted on a motorized X-Y translation stage normal to the incident laser beam. A large area of structured metal is obtained by scanning the laser spot across the metal surface at a certain velocity. In all cases structuring is performed near the ablation threshold. After irradiation the targets were rinsed with ethanol and dried at ambient temperature. The absorption spectra of the laser-exposed samples and liquid dispersions were taken using a UV-VIS spectrophotometer (*Perkin Elmer-Lambda 950*) equipped with an integrating sphere. The morphology of Al surface was studied by a field

emission scanning electron microscope (FE SEM) with a spatial resolution of 10 nm (*JEOL-JSM7000F*) and an atomic force microscope (*Digital Instruments, Nanoscope*), operating in non-contact mode. A Transmission Electron Microscope (*JEOL-100C*) was employed to image NP morphologies; a drop of a sample solution was placed on a copper grid and then dried at room temperature. X-ray diffraction (XRD) characterization was carried out using a diffractometer with Cu  $K\alpha$  X-rays (*Rigaku-RINT 2000*). Several tests were conducted on fluorescence on laser-exposed Al targets, using the 320 nm excitation beam of a He-Cd laser.

### 8.3 Coloration of Aluminum

Independently of the irradiation medium, the exposed surface of Al target acquires yellowish colour, being visible at angles close to normal incidence (**Figure 8.1**). The coloration is most pronounced in the case of exposure into ethanol, where it appears just after only a few pulses at a fluence of as low as  $0.05 \text{ J/cm}^2$  and a scanning speed of 0.5 mm/s. At lower fluences, virtually no changes of the Al surface are observed, even with elevated number of laser shots.

Higher scanning speeds of 4mm/s and a fluence of  $0.25 \text{ J/cm}^2$  are required to obtain similar coloration of the target under exposure in air. Colour changes are permanent, for instance, the target may be wiped by a wet tissue without any change of the colour and it is observed independently of the purity of Al target with Al content ranging from 75% through 95%. Hence, this coloration should be assigned to structuring of the Al surface at the nanometre scale similarly to previously reported NS on both Ag and Au [12, 13].

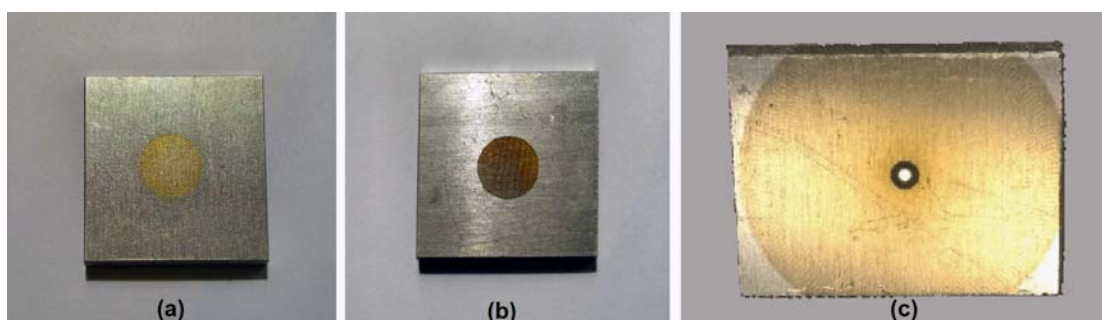


**Figure 8.1** : Macro view of an Al plate exposed to the radiation of a 180 fs-Ti:sapphire laser, in water (a) in ethanol (b) and in air (c), showing the yellow coloration of the target. For irradiation in water and ethanol, the fluence used was  $0.05 \text{ J/cm}^2$ . The corresponding fluence in air was  $0.25 \text{ J/cm}^2$ . In all cases, the exposure was performed through a contact mask.

**Figure 8.2** presents the absorption spectra of the Al surfaces structured with different laser sources. In the blue and near UV region the absorption of the exposed samples exceeds that of the initial surface while in the NIR range, the samples ablated into liquid show lower absorption. In all cases, the absorption maximum is situated around 300 nm, which is justified by the yellow coloration of the corresponding exposed areas. When the Al target is exposed into liquids the latter takes on a yellow colour as well (**Figure 8.3a**), indicating the formation of Al particles dispersed in the liquid. As shown in the spectrum of **Figure 8.3b**, these NP dispersions show a characteristic absorption peak close to 300nm. A TEM view of NP produced is presented in **Figure 8.3c**. These NP have a core-shell structure with a spherical shell and irregular core, with diameters ranging from 10 to 200 nm.

**Figures 8.4a, b** show FESEM images of the morphology of an Al target before and after the formation of nanostructures upon exposure into water and ethanol. The

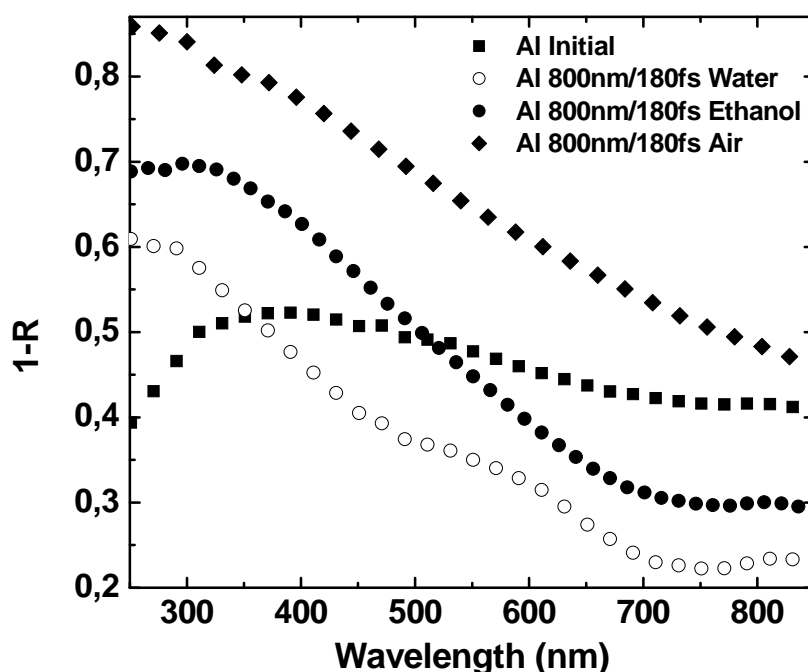


**Figure 8.2** : Absorption spectra of the initial Al surface and of those exposed to the radiation of a 180 fs laser. Reference reflector is Spectralon<sup>TM</sup>.

morphology obtained does not depend on the liquid environment used for ablation. A comparison between FESEM and AFM images from the same exposed surface are illustrated in **Figures 8.4b and c**. Both pictures indicate similar morphology, except for the mushroom-

like structures that are visible only by FESEM imaging. The bumps in the exposed Al surface have an average period of 200-300 nm, which corresponds to a density of  $\sim 10^9 \text{ cm}^{-2}$ .

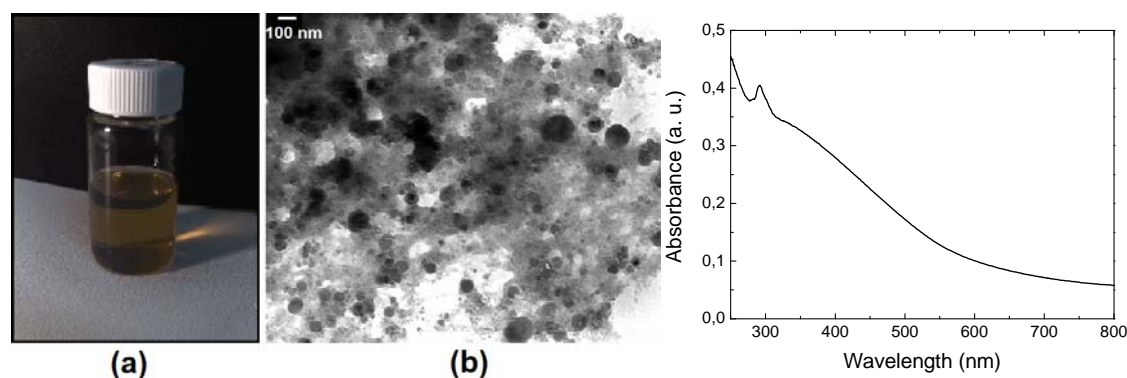


**Figure 8.3 :** (a) Macro view of Al NP dispersions generated in ethanol under ablation of an Al target using a 180 fs Ti:sapphire laser. (b) TEM image of NPs dispersed in ethanol (c) Optical absorption spectrum of the liquid dispersion; reference is pure ethanol.

No periodic ripples are visible that are typical of interference of the laser beam with Surface Electromagnetic Waves (SEW). This might be due to the fact that the initial Al surface has elevated roughness, and SEW rapidly damp in this surface. It should be noted here that the similarity of the absorption spectrum of the Al surface in a liquid and that of the liquid itself, obtained after ablation suggests that both spectra are due to similar nano-entities. In the case of the target these are nano-spikes (**Figure 8.4**) while the coloration of the liquid might be assigned to the formation of Al nanoparticles. Further studies are however required to elucidate this issue by investigating the properties of the dispersed particles.

On the other hand, the morphology of Al surface after ablation in air is pretty different from that after exposure into liquids. As depicted in **Figure 8.5**, in this case the irradiated surface comprises irregular nanoentities with an average size of 100 nm.

Similar coloration and associated NS are observed under exposure of duralumin at identical conditions. The absorption spectra of the exposed areas are virtually the same as in the case of pure Al, indicating their origin from the particular metal and not from impurities.

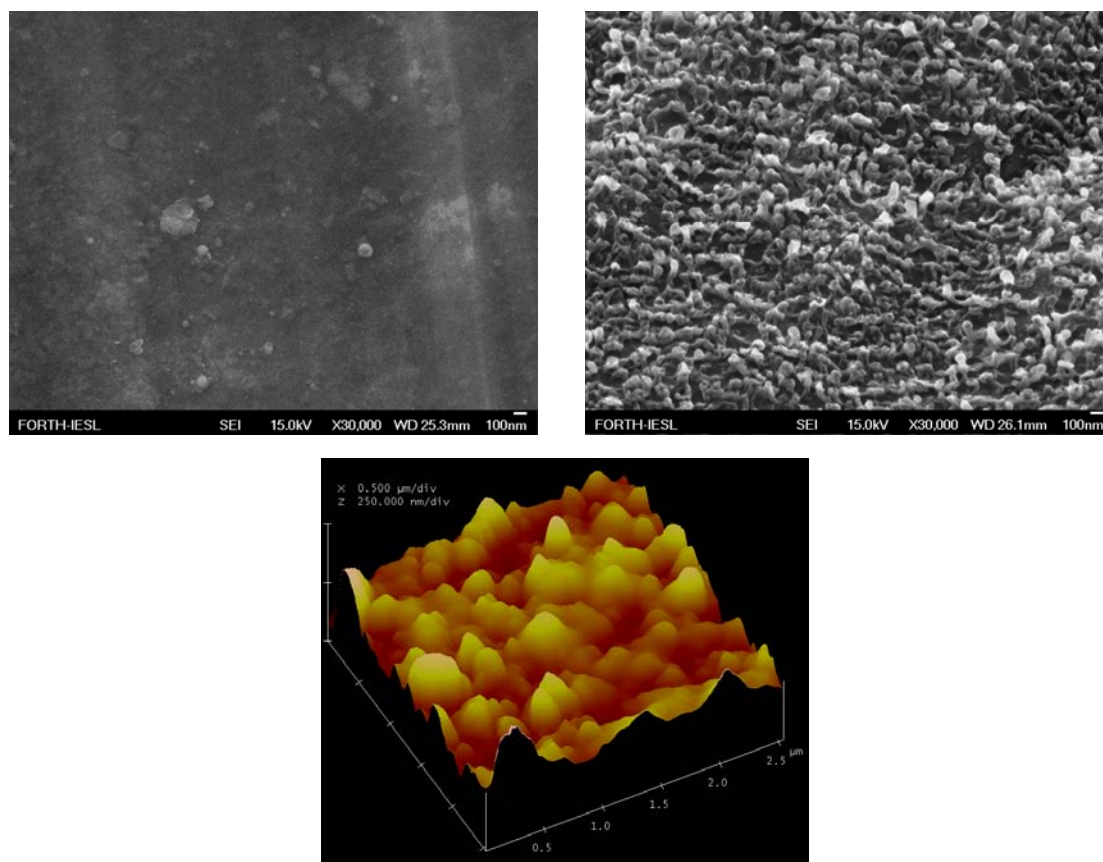


**Figure 8.4 :** FESEM view of a pristine (a) and laser exposed (b) surface of an Al target exposed to Ti:Sapphire fs laser radiation in liquid –water or ethanol- at a laser fluence of  $0.05 \text{ J/cm}^2$  and corresponding AFM image (c). The AFM image Z-scale is 250 nm/division.

## 8.4 Formation of NS

The spectral features and therefore the coloration of the Al exposed to fs pulses under a layer of liquid may be attributed to the formation of NS on its surface. Similarly to previously observed coloration of Ag under its ablation in liquids, these nano-bumps confine the oscillations of free electrons as soon as their height exceeds the electron mean free path. The theoretical position of plasmon resonance of Al NP of 10 nm in diameter in water was calculated in [19], and the maximum of absorption lies around 200 nm. However, it is red-shifted for NP of higher diameters [19, 20]. Also, oxidation of Al NP would also cause a red shift of their plasmon resonance, since its oxide,  $\text{Al}_2\text{O}_3$ , has higher refractive index in the UV range than water. It should be noted that oxide itself has no absorption in the range of study

since its absorption only commences from 250 nm and even shorter wavelength, depending on its impurities. The presence of aluminum oxide is indicated by fluorescence measurements performed on the exposed surfaces (not presented here for brevity), showing that the corresponding emission intensity is several times lower in the case of exposure under ethanol than in water. This oxide layer may be formed by fast oxidation of the irradiated surface upon solidification and efficiently passivates the surface of NS against further oxidation, so they are chemically stable to provide permanent coloration of Al surface. No fluorescence is detected in the case of a pristine Al target.

The mechanism of formation of nano-bumps still remains to be clarified. NS on Al have nothing to do with periodic ripples usually observed in experiments on laser exposure of solids, since their period does not depend on the laser wavelength. This is also confirmed by the fact that we have never observed ripples upon FE SEM imaging of the exposed areas. Capillary forces are also excluded since they lead to the formation of large-scale periodic structures having a period of the order of 10  $\mu\text{m}$  [21, 22]. In contrast, the formation of self-organized NS on Al proceeds on a roughened surface in a similar way to what was previously reported for NS on Ag and Au [12, 13, 18]. In particular, NS creation has been tentatively assigned to the instability at the interface between metal melt and liquid vapour. At this point the initial micro-relief on the target surface may serve as a natural boundary for formation of nanoscale bumps. Another specific feature of ablation under a liquid layer is the action of a pressure wave onto the target. The origin of this wave in the case of short laser pulses is the recoil pressure of the liquid surrounding the laser [12, 18]. The expanding vapors expel the molten layer, which then solidifies.

The similarity of the spectrum under ablation of Al with fs laser pulses in air and in liquids suggests that the mechanism behind the NS formation is the same, independently on the environment. In all cases the NS appear as a result of action of recoil pressure onto a thin molten layer on Al. When the exposure is performed in liquids this pressure is the pressure of vapor of the surrounding liquid. In case of exposure in air this pressure is due to fast evaporation of the molten layer itself. Accordingly, the formation of NS on Al in air and under a liquid layer requires different laser fluence on the target surface. In case of exposure in air, this fluence is several times higher than in liquid environment.

## **8.5 Conclusions**

NS formation on bulk Al has been experimentally studied under its ablation in either liquid or air with fs laser pulses. The formation of such NS on Al modifies its absorption spectrum in the UV-Vis range. Namely, the absorption increases substantially while its wings extending to the visible result in a yellow coloration of the exposed surface. This change in the optical properties attributed to the fact that the nano-bumps formed confine the oscillations of free electrons exhibiting their plasmon resonance absorption peak from deep UV to visible range of spectrum. Interestingly, the formation of nano-reliefs on the Al surface is realised by just a few short laser pulses. In view of this, the described process of NS formation can be considered as an efficient method for direct laser writing of NS, since high production rates on extended surfaces can be obtained within reasonable processing time.

## 6. References

1. D. Schmeiber, O. Bohme, A. Yfantis, T. Heller, D.R. Batchelor, I. Lundstorm, L. Spetz, *Phys. Rev. Lett.* 83, (1999) 2380.
2. Y. Xiong, J. Chen, B. Wiley, Y. Xia, Y. Yin, Z. Li, *Nano Lett.* 5, (2005) 1237.
3. Y.W.C. Cao, R.C. Jin, C.A. Mirkin, *Science* 297 (2002) 1536.
4. J.J. Diao, J. Sun, J.B. Hutchison, *Appl. Phys. Lett.* 87, (2005)103 113.
5. N.V. Tarasenko, A.V. Butsen, E.A. Nevar, *Appl. Surf. Sci.* 247, (2005)418.
6. F.J. Garcia-Vidal, J.B. Pendry, *Phys. Rev. Lett.* 77 (1996) 1163.
7. C.K. Chen, A.R.B. de Castro, Y.R. Shen, *Phys. Rev. Lett.* 46 (1981) 145.
8. X. Yin, N. Fang, X. Zhang, I.B. Martini, B.J. Schwartz, *Appl. Phys. Lett.* 81 (2002) 3663.
9. C. Wen, K. Ishikawa, M. Kishima, K. Yamada, *Sol. Energy Mater. Sol.Cells* 61 (2000) 339.
10. J. Suna, S.L. Simon, *Thermochimica Acta* 463 (2007) 32–40.
11. P.V. Kazakevich, A.V. Simakin, V.V. Voronov, and G.A. Shafeev, *Applied Surface Science*, 252 (2006) 4373–4380.
12. E.V. Zavedeev, A.V. Petrovskaya, A.V. Simakin, and G.A. Shafeev, *Quantum Electronics*, 36 (2006) 978-980.
13. S. Lau Truong, G. Levi, F. Bozon-Verduraz, A.V. Petrovskaya, A.V. Simakin, and G.A. Shafeev, *Appl. Phys.* A89 (2007) 373 – 376.
14. K. Park, A. Rai and M.R. Zachariah, *Journal of Nanoparticle Research* 8 (2006) 455–464.
15. K. Tanabe, *Materials Letters* 61 (2007) 4573–4575.
16. C. Langhammer, M. Schwind, B. Kasemo, and I. Zoric, *Nanoletters* 8 (2008) 1461-1471.
17. Park K., D. Lee, A. Rai, R. Mukherjee & M.R. Zachariah. *J. Phys. Chem. B* 109, (2005) 7290–7299.
18. G. W. Yang, *Progress in Materials Science* 52 (2007) 648- 698.
19. J.A. Creighton and D.G. Eadon, *J. Chem. Soc. Faraday Trans.*, 87, (1991) 3881.
20. G. L. Hornyak, K. L. N. Phani, D. L. Kunked, V. P. Menon and C. R. Martin, *Nanostructured Materials*, 6, (1995) 839.
21. V. Zorba, P. Tzanetakakis, C. Fotakis, E. Spanakis, E. Stratakis, D. G. Papazoglou, I. Zergioti, *Appl. Phys. Lett.*, 88 (2006) 081103.
22. V. V. Voronov, S.I. Dolgaev, S.V. Lavrishev, A.A. Lyalin, A.V. Simakin, and G.A. Shafeev, *Appl.Phys.* A73 (2001) 177-181.